ADMET & DMPK **14** (2026) 3520*; doi: https://doi.org/10.5599/admet.3520*

ADMET
Open Access : ISSN : 1848-7718
http://www.pub.iapchem.org/ojs/index.php/admet

Original scientific paper

Novel hydroxynaphthalene and quinoline derivatives effective against *Trypanosoma* and *Leishmania*

Tomas Gonec[1], Tomas Strharsky[1], Marcela Vettorazzi[2], Lucas Gutierrez[2], Martina Cudova[3], Tereza Kauerova[3], Michaela Simurdova[4], Michal Oravec[5], Jiri Kos[4,*], Peter Kollar[3], Bohuslav Drahos[6], Jan Jurica[7], Ondrej Zendulka[7], Jana Gregorova[4], Ondrej Pes[4], Joelle Quetin-Leclercq[8], Josef Jampilek[9,10] and Ricardo D. Enriz[2,★]

[1]*Department of Chemical Drugs, Faculty of Pharmacy, Masaryk University, Palackeho 1946/1, 612 00 Brno, Czech Republic*
[2]*Faculty of Chemistry, Biochemistry and Pharmacy, National University of San Luis. IMIBIO-CONICET, Ejército de los Andes 950 (5700) San Luis, Argentina*
[3]*Department of Pharmacology and Toxicology, Faculty of Pharmacy, Masaryk University, Palackeho tr. 1946/1, 612 00 Brno, Czech Republic*
[4]*Department of Biochemistry, Faculty of Medicine, Masaryk University, Kamenice 5, Brno 625 00, Czech Republic*
[5]*Global Change Research Institute CAS, Belidla 986/4a, 603 00 Brno, Czech Republic*
[6]*Department of Inorganic Chemistry, Faculty of Science, Palacký University Olomouc, 17. listopadu 12, 779 00 Olomouc, Czech Republic*
[7]*Department of Pharmacology, Faculty of Medicine, Masaryk University, Kamenice 5, 625 00 Brno, Czech Republic*
[8]*Louvain Drug Research Institute, Pharmacognosy Laboratory, UCLouvain, Avenue E. Mounier, 72, B1.7203, B-1200 Brussels; Belgium*
[9]*Department of Chemical Biology, Faculty of Science, Palacky University Olomouc, Slechtitelu 27, 78371 Olomouc, Czech Republic*
[10]*Institute of Chemistry, University of Silesia, Szkolna 9, 40-007 Katowice, Poland*

Corresponding Author: E-mail: *jirikos85@gmail.com; ★denriz@unsl.edu.ar

Received: June 16, 2026; Revised: August 8, 2026; Published: August 20, 2026

Abstract

Background and purpose: The increasing prevalence of multidrug-resistant parasites, particularly *Trypanosoma* and *Leishmania*, together with the limited efficacy of current therapies, highlights the need for new antiprotozoal agents. Current therapeutic options remain limited by toxicity and insufficient efficacy. Building on our previous work on naphthalene and quinoline derivatives with antiparasitic activity, we report new derivatives with potent antiprotozoal activity against both *Leishmania mexicana* and *Trypanosoma brucei*. **Experimental approach:** The synthesized compounds were evaluated for their antiprotozoal activity against *Leishmania mexicana* and *Trypanosoma brucei*, cytotoxicity, and metabolic stability in rat and human liver microsomes. To investigate their possible mechanism of action, a comprehensive molecular modelling study was performed, including molecular docking, molecular dynamics simulations (*per*-residue analysis), and quantum theory of atoms in molecules (QTAIM) calculations. **Key results:** Some synthesized compounds exhibited inhibitory effects comparable to or greater than those of the reference compounds and showed no significant cytotoxicity. The most active molecules demonstrated high metabolic stability in both rat and human liver microsomes. Molecular modelling provided mechanistic insight into the observed antiparasitic activity and identified trypanothione reductase and arginase as possible molecular targets in *Leishmania mexicana*. For *Trypanosoma brucei*, our simulations suggest that trypanothione reductase is the most probable molecular target and that these compounds inhibit this enzyme. **Conclusion:** The synthesized hydroxynaphthalene and quinoline derivatives represent promising antiprotozoal compounds with favourable metabolic stability and low cytotoxicity. Molecular modelling provided a possible explanation for

their biological activity and suggested potential molecular targets that may support their further optimization.

©2026 by the authors. This article is an open-access article distributed under the terms and conditions of the Creative Commons Attribution license (http://creativecommons.org/licenses/by/4.0/).

Keywords

Carboxanilides; antiprotozoal activity; structure-activity relationship; metabolic stability; cytotoxicity; molecular modelling

Introduction

Rising global temperatures combined with the increasing frequency of extreme weather events such as floods, droughts, and heatwaves have significantly affected the transmission patterns of vector-borne infectious diseases [1,2]. These environmental changes are facilitating the spread of diseases like malaria and Lyme borreliosis into new geographic areas, including higher latitudes that were previously considered unsuitable for their occurrence [2]. For example, *Aedes aegypti* and *Aedes albopictus*, the principal vectors responsible for transmitting dengue, chikungunya and Zika viruses, have extended their geographic range into regions previously considered inhospitable, including areas of Europe and North America. This range expansion is associated with a rise in the population at risk; projections estimate that climate change alone could expose an additional 298 to 460 million people, representing an increase of 8 to 12 percent in the vulnerable population [2-4]. In response, the Global Vector Control Response (GVCR) 2017-2030 was endorsed by the World Health Assembly in 2017 [5]. It provides strategic guidance for countries and development partners to urgently strengthen vector control as a fundamental approach to disease prevention and epidemic response [5,6].

Vector-borne diseases account for more than 17 % of all infectious diseases and cause over 700,000 deaths annually [5-7]. They can be caused by parasites, bacteria, or viruses. The increasing prevalence of multidrug-resistant parasites, combined with a growing immunodeficiency in the human population [8], contributes to a further rise in infections caused by opportunistic pathogens, posing a significant global challenge. This group includes major protozoan pathogens, particularly those of the genera *Trypanosoma* and *Leishmania*, which represent key etiological agents in zoonotic infections affecting human populations in endemic regions. These parasites share a common developmental stage in their life cycles that thrives by exploiting the human host for replication and reproduction. While malaria caused by the genus *Plasmodium* remains the most severe disease, human African trypanosomiasis (sleeping sickness) and leishmaniasis are often classified as neglected tropical diseases [7,9-11].

Human African trypanosomiasis (HAT) is a parasitic disease transmitted by the tsetse fly in Sub-Saharan Africa. It is caused by the parasite *Trypanosoma brucei gambiense* (a slow-progressing disease in western and central Africa) and *T.b. rhodesiense* (a fast-progressing disease in eastern and southern Africa). Without treatment, HAT is fatal. Pentamidine, eflornithine or their combination with nifurtimox, and fexinidazole (the only oral drug) have been approved for the treatment of HAT caused by *T.b. gambiense*. Suramin is indicated for the first phase of infection caused by *T.b. rhodesiense*, and melarsoprol is indicated for the second phase. In addition, of these six drugs, five of which are administered intravenously or intramuscularly, four are associated with significant adverse effects, highlighting the need for further research into safer and more effective therapies [12,13].

Leishmaniasis is a parasitic disease caused by protozoa of the genus *Leishmania*, which is transmitted to humans by the bite of sandflies of the genera *Phlebotomus* and *Lutzomyia*. The disease occurs in tropical and subtropical regions of the world and, although it is the second most widespread parasitic disease after

malaria (with a global annual incidence of up to 1 million new cases), it is considered a neglected tropical disease. There are three forms of leishmaniasis: cutaneous (causing skin ulcers), mucocutaneous (affecting the skin, nose, mouth, and throat), and visceral (a systemic, fatal disease). Treatment is complicated and often unsuccessful. There is high resistance to the used drugs sodium stibogluconate and meglumine antimoniate; the drugs are administered intramuscularly and are highly toxic. Alternatively, drugs developed for the treatment of other diseases, such as amphotericin (an antifungal), miltefosine (an antineoplastic) or paromomycin (an antibiotic), can be used [14-16].

A wide range of novel naphthalene and quinoline derivatives synthesized in recent years have demonstrated potent antileishmanial and/or antitrypanosomal activity [17-22]. Over the past two decades, our research group has significantly contributed to the exploration of these structural classes by developing a large library of novel compounds, particularly with anticancer, antibacterial and antifungal properties [23-28]. Among these efforts, we have synthesized a series of 3-hydroxy-2-naphthoylanilide derivatives, several of which exhibited notable antitrypanosomal activity [29]. Although naphthoic acid derivatives exhibited promising antiparasitic activity, further progress required systematic modulation of key physicochemical properties, such as lipophilicity, electronic distribution, and hydrogen-bonding capacity, which are critical for biological efficacy and pharmacokinetic behaviour. To achieve broader structural diversity and greater control over these parameters, we shifted our focus to (*E*)-prop-1-en-1-ylbenzene derivatives, as reported in [30-33]. This shift enabled a more detailed investigation of the structure-activity relationship and facilitated the optimization of novel compounds with improved antiprotozoal properties. A comparable structure-activity relationship was observed, in which high antiprotosoic potency was associated with the presence of a trifluoromethyl group at the *meta* or *para* position of the aniline ring. Moreover, compounds bearing symmetrical disubstitution with trifluoromethyl groups at these positions exhibited similarly enhanced activity, reinforcing the relevance of specific substitution patterns for optimizing antiprotozoal efficacy. The promising antiprotozoal activity observed in these derivatives prompted us to revisit and further modify the core naphthoylanilide scaffold. Based on our previous findings, the specific substitution pattern on the aniline ring can be regarded as a privileged structural motif for antiparasitic activity. With the aim of developing potent compounds against *Leishmania* spp. and *Trypanosoma* spp., we systematically explored structural variations within this framework to optimize efficacy while preserving the favourable substitution characteristics identified in earlier studies. Based on our studies, we report here new structures with potent activity against both *Leishmania* spp. and *Trypanosoma* spp., making them excellent candidates for therapeutic agents. Furthermore, our molecular simulation results enabled us to propose potential molecular targets for these compounds in both parasites.

Collectively, the present work extends our previous studies not merely by expanding this chemical series to include new unique, previously undescribed molecules, but by integrating biological evaluation with advanced molecular modelling to establish experimentally supported structure-activity relationships and propose a possible molecular mechanism underlying the observed antiparasitic activity.

Materials and methods

Chemistry

General

All reagents were purchased from Merck (Sigma-Aldrich, St. Louis, MO, USA) and Alfa (Alfa-Aesar, Ward Hill, MA, USA). Microwave-assisted reactions were performed using a StartSYNTH microwave lab station (Milestone, Sorisole, BG, Italy). Melting points were determined on a Kofler hot-plate apparatus HMK (Franz

Kustner Nacht KG, Dresden, Germany) and were not corrected. Infrared (IR) spectra were recorded on an ATR diamond iD7 for a Nicolet™ Impact 410 Fourier-transform IR spectrometer (Thermo Scientific, West Palm Beach, FL, USA). The spectra were obtained by accumulating 64 scans at a resolution of 2 cm^{-1} over the region 4000-650 cm^{-1}. All ^{1}H- and ^{13}C-NMR spectra were recorded on a JEOL ECZR 400 MHz NMR spectrometer (400 MHz for ^{1}H and 100 MHz for ^{13}C, Jeol, Tokyo, Japan) in dimethyl sulfoxide-d_6 (DMSO-d_6) or acetonitrile-d_3 (CD_3CN). ^{1}H and ^{13}C chemical shifts (δ) are reported in ppm. High-resolution mass spectra were measured using a high-performance liquid chromatograph Dionex UltiMate® 3000 (Thermo Scientific, West Palm Beach, FL, USA) coupled with an LTQ Orbitrap XL™ Hybrid Ion Trap-Orbitrap Fourier-transform mass spectrometer (Thermo Scientific) equipped with a HESI II (heated electrospray ionization) source in the negative mode.

General procedure for synthesis of carboxamides **1a**-**4d**

Carboxylic acid (2.64 mM) was suspended in dry chlorobenzene (25 mL) at ambient temperature and phosphorus trichloride (0.12 mL, 1.32 mM, 0.5 eq.), and the corresponding substituted aniline (2.64 mM, 1 eq.) was added dropwise. The reaction mixture was transferred to the microwave reactor, where the synthesis was performed (1st phase: 10 min, 100 °C; 2nd phase: 15 min, 120 °C; 3rd phase: 20 min, 130 °C, 500 W). Then, the mixture was cooled to 60 °C, and the solvent was removed under reduced pressure to dryness. The residue was washed with hydrochloric acid and water. The crude product was recrystallized from diluted EtOH.

Ring-substituted 2-hydroxynaphthalene-1-carboxanilides **1a** and **1b** were previously prepared and characterized by Gonec *et al*. [34]; 1-hydroxynaphthalene-2-carboxanilides **2a**-**2d** were characterized in [23,35,36].

N-[3,5-bis(trifluoromethyl)phenyl]-2-hydroxynaphthalene-1-carboxamide (**1c**). Yield 57 %; mp 178-179 °C; IR (cm^{-1}): 3097, 1637, 1567, 1542, 1512, 1471, 1439, 1368, 1348, 1273, 1183, 1165, 1124, 972, 933, 885, 823, 756, 699, 681; ^{1}H-NMR (DMSO-d_6), δ: 11.09 (s, 1H), 10.31 (s, 1H), 8.50 (s, 2H), 7.92 (d, 1H, *J*=8.4 Hz), 7.89 (s, 1H), 7.84 (d, 1H, *J*=5.9 Hz), 7.72 (d, 1H, *J*=8.4 Hz), 7.48 (td, 1H, *J*=7.6 Hz, *J*=1.1 Hz), 7.35 (td, 1H, *J*=8.1 Hz, *J*=1.1 Hz), 7.28 (d, 1H, *J*=8.8 Hz) (Supplementary material, Figure S1); ^{13}C-NMR (DMSO-d_6), δ: 166.80, 152.01, 141.33, 131.81, 131.16, 130.87, 130.84, 128.05, 127.34, 127.29, 123.21, 123.21, 118.86, 118.28, 117.38, 116.16 (Figure S2, S3); HR-MS: $C_{19}H_{10}F_6NO_2$ $[M-H]^-$ calculated 398.06212 *m*/*z*, found 398.06140 *m*/*z* (Figure S4).

N-(3,5-dichlorophenyl)-2-hydroxynaphthalene-1-carboxamide (**1d**). Yield 67 %; mp 246-249 °C; IR (cm^{-1}): 3362, 1646, 1586, 1538, 1514, 1448, 1436, 1403, 1352, 1312, 1299, 1262, 1231, 1211, 1114, 966, 838, 806, 795, 745, 665; ^{1}H-NMR (DMSO-d_6), δ: 10.77 (s, 1H), 10.26 (s, 1H), 7.90 (d, 2H, *J*=4.4 Hz), 7.86 (d, 2H, *J*=7.7 Hz), 7.67 (d, 1H, *J*=8.4 Hz), 7.48 (td, 1H, *J*=7.8, *J*=1.1 Hz), 7.34 (td, 1H, *J*=7.5 Hz, *J*=1.1 Hz), 7.33 (s, 1H), 7.26 (d, 1H, *J*=8.8 Hz) (Figure S5); ^{13}C-NMR (DMSO-d_6), δ: 166.42, 151.87, 141.81, 134.14, 131.18, 130.66, 128.04, 127.34, 127.23, 123.19, 123.17, 122.54, 118.28, 117.70, 117.32 (Figure S6, S7); HR-MS: $C_{17}H_{10}Cl_2NO_2$ $[M-H]^-$ calculated 330.00941 *m*/*z*, found 330.00946 *m*/*z* (Figure S8).

4-hydroxy-*N*-[3-(trifluoromethyl)phenyl]quinoline-3-carboxamide (**3a**). Yield 75 %; mp 280-285 °C; IR (cm^{-1}): 3064; 2911; 1669; 1622; 1599; 1580; 1515; 1475; 1451; 1360; 1336; 1308; 1284; 1269; 1250; 1212; 1165; 1147; 1117; 1092; 1069; 1026; 899; 822; 785; 761; 747; 695; 684; ^{1}H-NMR (DMSO-d_6), δ: 13.01 (br. s, 1H); 12.57 (s, 1H); 8.87 (s, 1H); 8.30-8.33 (m, 2H); 7.79-7.83 (m, 2H); 7.72-7.75 (m, 1H); 7.58 (t, *J*=7.8 Hz, 1H); 7.51-7.55 (m, 1H); 7.43 (d, *J*=7.8 Hz, 1H) (Figure S9); ^{13}C-NMR (DMSO-d_6), δ: 176.34; 163.40; 144.35; 139.50; 139.08; 133.11; 130.17; 129.68 (q, *J*=31.8 Hz); 125.88; 125.44; 125.43; 124.13 (q, *J*=272.6 Hz); 123.22; 119.70 (q, *J*=3.9 Hz); 119.24; 115.70 (q, *J*=3.9 Hz) (Figure S10, S11); 110.11; HR-MS: $C_{17}H_{10}F_3N_2O_2$ $[M-H]^-$ calculated 331.06999 *m*/*z*, found 331.07047 *m*/*z* (Figure S12).

(cc) BY

4-hydroxy-*N*-[4-(trifluoromethyl)phenyl]quinoline-3-carboxamide (**3b**). Yield 58 %; mp 286-290 °C; IR (cm^{-1}): 3064; 2981; 2915; 1662; 1600; 1551; 1523; 1475; 1445; 1415; 1318; 1305; 1259; 1215; 1164; 1151; 1105; 1063; 1014; 821; 761; 749; 685; ^{1}H-NMR (DMSO-d_6), δ: 13.03 (br. s, 1H); 12.81 (s, 1H); 8.90 (s, 1H); 8.33 (dd, *J*=8.2 Hz, *J*=1.4 Hz, 1H); 7.95 (d, *J*=8.2 Hz, 2H); 7.80-7.85 (m, 1H); 7.74-7.77 (m, 1H); 7.72 (d, *J*=8.7 Hz, 2H); 7.55 (ddd, *J*=8.2 Hz, *J*=6.9 Hz, *J*=1.4 Hz, 1H) (Figure S13); ^{13}C-NMR (DMSO-d_6), δ: 176.37; 163.38; 144.48; 142.30 (q, *J*=1.9 Hz); 139.08; 133.15; 126.29 (q, *J*=3.9 Hz); 125.88; 125.48; 125.45; 124.46 (q, *J*=273.6 Hz); 123.31 (q, *J*=31.8 Hz); 119.55; 119.27; 110.10 (Figure S14, S15); HR-MS: $C_{17}H_{10}F_3N_2O_2$ $[M-H]^-$ calculated 331.06999 *m*/*z*, found 331.07040 *m*/*z* (Figure S16).

N-[3,5-bis(trifluoromethyl)phenyl]-4-oxo-1,4-dihydroquinoline-3-carboxamide (**3c**). Yield 59 %; mp 302--305 °C; IR (cm^{-1}): 2952; 1661; 1626; 1580; 1558; 1539; 1471; 1451; 1386; 1354; 1308; 1277; 1267; 1214; 1171; 1150; 1118; 1040; 993; 935; 881; 849; 764; 701; 682; ^{1}H-NMR (DMSO-d_6), δ: 13.04 (br. d, 1H, *J*=5.9 Hz); 12.96 (s, 1H); 8.86 (d, 1H, *J*=6.9 Hz); 8.40 (s, 2H); 8.28 (d, 1H, *J*=7.3 Hz); 7.77-7.82 (m, 1H); 7.70-7.75 (m, 2H); 7.53 (ddd, 1H, *J*=8.2 Hz, *J*=6.9 Hz, *J*=0.9 Hz) (Figure S17); ^{13}C-NMR (DMSO-d_6), δ: 176.30; 163.92; 144.62; 140.55; 139.07; 133.27; 130.89 (q, *J*=31.8 Hz); 125.84; 125.63; 125.39; 123.25 (q, *J*=272.6 Hz); 119.63 (m); 119.33; 116.18 (m); 109.70 (Figure S18, S19); HR-MS: $C_{18}H_9F_6N_2O_2$ $[M-H]^-$ calculated 399.05737 *m*/*z*. found 399.05795 *m*/*z* (Figure S20).

N-(3,5-dichlorophenyl)-4-oxo-1,4-dihydroquinoline-3-carboxamide (**3d**). Yield 73 %; mp 305-309 °C; IR (cm^{-1}): 2979; 1669; 1623; 1582; 1515; 1472; 1444; 1411; 1347; 1293; 1254; 1207; 1180; 1148; 1109; 1022; 990; 925; 868; 836; 792; 753; ^{1}H-NMR (DMSO-d_6), δ: 13.04 (br. d, 1H, *J*=4.6 Hz); 12.73 (s, 1H); 8.85 (d, 1H, *J*=6.4 Hz); 8.30 (d, 1H, *J*=8.2 Hz); 7.79-7.84 (m, 3H); 7.73-7.76 (m, 1H); 7.54 (t, 1H, *J*=7.5 Hz); 7.28 (t, 1H, *J*=1.8 Hz) (Figure S21); ^{13}C-NMR (DMSO-d_6), δ: 176.31; 163.51; 144.48; 141.02; 139.07; 134.26; 133.20; 125.84; 125.55; 125.43; 122.60; 119.29; 117.89; 109.86 (Figure S22, S23); HR-MS: $C_{16}H_9Cl_2N_2O_2[M-H]^-$ calculated 331.00466 *m*/*z*, found 331.00546 *m*/*z* (Figure S24).

4-hydroxy-7-(trifluoromethyl)-*N*-[3-(trifluoromethyl)phenyl]quinoline-3-carboxamide (**4a**). Yield 78 %; mp 280-284 °C; IR (cm^{-1}): 3339; 2944; 2832; 1662; 1605; 1559; 1522; 1475; 1453; 1417; 1371; 1335; 1317; 1171; 1126; 1067; 1032; 901; 785; 741; ^{1}H-NMR (DMSO-d_6), δ: 13.17 (br. s, 1H); 12.45 (s, 1H); 8.99 (s, 1H); 8.45 (d, 1H, *J*=8.7 Hz); 8.28 (s, 1H); 8.06 (s, 1H); 7.76-7.81 (m, 2H); 7.57 (t, 1H, *J*=8.0 Hz); 7.42 (d, 1H, *J*=7.8 Hz) (Figure S25); ^{13}C-NMR (DMSO-d_6), δ: 175.62; 162.83; 145.64; 139.26; 138.77; 132.38 (q, *J*=31.8 Hz); 130.14; 129.65 (q, *J*=31.8 Hz); 128.08; 127.36; 124.08 (q, *J*=272.6 Hz); 123.44 (q, *J*=272.6 Hz); 123.23; 120.97 (q, *J*=2.9 Hz); 119.84 (q, *J*=3.9 Hz); 116.85 (q, *J*=3.9 Hz); 115.72 (q, *J*=4.8 Hz); 111.23 (Figure S26, S27); HR-MS: $C_{18}H_9F_6N_2O_2$ $[M-H]^-$ calculated 399.05737 *m*/*z*, found 399.05746 *m*/*z* (Figure S28).

4-hydroxy-7-(trifluoromethyl)-*N*-[4-(trifluoromethyl)phenyl]quinoline-3-carboxamide (**4b**). Yield 77 %; mp 317-320 °C; IR (cm^{-1}): 3326; 2943; 2830; 1681; 1612; 1534; 1453; 1415; 1370; 1318; 1179; 1134; 1115; 1062; 1031; 889; 846; 827; 805; 740; ^{1}H-NMR (DMSO-d_6), δ: 13.18 (br. s, 1H); 12.53 (s, 1H); 9.02 (s, 1H); 8.48 (d, 1H, *J*=8.3 Hz); 8.08 (s, 1H); 7.91 (d, 2H, *J*=8.8 Hz); 7.41 (d, 1H, *J*=8.7 Hz); 7.70 (d, 2H, *J*=8.8 Hz) (Figure S29); ^{13}C-NMR (DMSO-d_6), δ: 175.69; 162.87; 145.84; 142.09; 138.84; 132.42 (q, *J*=32.8 Hz); 128.13; 127.41; 126.27 (q, *J*=2.9 Hz); 124.98 (q, *J*=272.6 Hz); 124.36 (q, *J*=272.6 Hz); 123.48 (q, *J*=32.8 Hz); 121.04 (q, *J*=2.9 Hz); 119.59; 116.93 (q, *J*=2.9 Hz); 111.26 (Figure S30, S31); HR-MS: $C_{19}H_9F_9N_2O_2$ $[M-H]^-$ calculated 399.05737 m/z, found 399.05740 m/z (Figure S32).

N-[3,5-bis(Trifluoromethyl)phenyl]-4-hydroxy-7-(trifluoromethyl)quinoline-3-carboxamide (**4c**). Yield 79 %; mp 316-319 °C; IR (cm^{-1}): 3278; 3091; 2948; 1668; 1609; 1557; 1532; 1471; 1448; 1386; 1364; 1317; 1266; 1168; 1126; 1111; 1066; 882; 863; 834; 806; 742; 699; 683; ^{1}H-NMR (CD_3CN), δ: 12.62 (s, 1H); 10.79 (br. s, 1H); 8.88 (s, 1H); 8.48 (d, 1H, *J*=8.4 Hz); 8.30 (s, 2H); 7.92 (s, 1H); 7.69 (d, 1H, *J*=8.4 Hz); 7.66 (s, 1H) (Figure

S33); ^{13}C-NMR (CD_3CN), *δ*: 177.80; 164.84; 146.71; 141.91; 140.07; 135.10; 134.60 (q, *J*=32.2 Hz); 132.84 (q, *J*=33.0 Hz); 129.81; 128.89; 124.90 (q, *J*=271.3 Hz); 124.84 (q, *J*=272.7 Hz); 122.57 (q, *J*=3.5 Hz); 121.20 (q, *J*=4.2 Hz); 117.88 (m); 113.02 (Figure S34, S35); HR-MS: $C_{19}H_8F_9N_2O_2$ $[M-H]^-$ calculated 467.04476 *m*/*z*, found 467.04593 *m*/*z* (Figure S36).

N-(3,5-dichlorophenyl)-4-hydroxy-7-(trifluoromethyl)quinoline-3-carboxamide (**4d**). Yield 73 %; mp 324-327 °C; IR (cm^{-1}): 3346; 2945; 2916; 2833; 1658; 1612; 1584; 1521; 1474; 1439; 1413; 1367; 1312; 1280; 1182; 1133; 1109; 1066; 1037; 913; 891; 856; 837; 800; 780; 742; ^{1}H-NMR (DMSO-d_6), *δ*: 13.19 (br. s, 1H); 12.44 (s, 1H); 8.99 (s, 1H); 8.46 (d, 1H, *J*=8.2 Hz); 8.09 (s, 1H); 7.79-7.83 (m, 3H); 7.27 (s, 1H) (Figure S37); ^{13}C-NMR (DMSO-d_6), *δ*: 175.53; 162.90; 145.72; 140.73; 138.71; 134.19; 132.38 (q, *J*=32.8 Hz); 128.00; 127.32; 123.43 (q, *J*=272.6 Hz); 122.68; 121.01 (q, *J*=2.9 Hz); 117.81; 116.82 (q, *J*=4.8 Hz); 110.95 (Figure S38, S39); HR-MS: $C_{17}H_8Cl_2F_3N_2O_2$ $[M-H]^-$ calculated 398.99204 *m*/*z*, found 398.99310 *m*/*z* (Figure S40).

Lipophilicity determination by HPLC

An Agilent 1200 HPLC system equipped with a DAD detector (Agilent, Santa Clara, CA, USA) was used. A chromatographic column Symmetry® C_{18} 5 µm, 4.6×250 mm, part No. WAT054275 (Waters Corp., Milford, MA, USA) was used. The HPLC separation process was monitored and evaluated with EZChrom Elite software ver. 3.3.2 (Agilent). Isocratic elution with a mixture of MeOH p.a. (72 %) and H_2O-HPLC Milli-Q grade (28 %) as a mobile phase was used. The total flow of the column was 1.0 mL min^{-1}, injection 20 µL, column temperature 40 °C and sample temperature 10 °C. The detection wavelength of 0.21 nm was chosen. The KI methanolic solution was used for the dead time (t_D) determination. Retention times (t_R) were measured in minutes. The capacity factors *k* was calculated according to the formula $k = (t_R - t_D)/t_D$, where t_R is the retention time of the solute, whereas t_D denotes the dead time obtained using an unretained analyte. Log *k*, calculated from the capacity factor *k*, is used as the lipophilicity index converted to the log *P* scale.

Crystal data

Single crystals of compound **4c** suitable for X-ray structure analysis were prepared by slow evaporation of the saturated solution of **4c** in acetonitrile. X-ray diffraction data were collected on XtaLAB Synergy-i (Rigaku) diffractometer equipped with a HiPix 3000 Bantam detector and a monochromatized microfocus PhotonJet-i CuKα radiation source (*λ* = 0.154184 nm) at 100 K. The molecular structure of the studied compound was solved by direct methods and refined by a full-matrix least-squares procedure SHELXL [37], in the program Olex2 [38]. The hydrogen atoms on carbon atoms were fixed into idealized positions (riding model) and assigned temperature factors of $U_{iso}(H)=1.2U_{eq}(CH, CH_2)$. The molecular structure of the compound studied was drawn using Mercury software [39].

Bioassays and toxicity

In vitro antiparasitic activity evaluation

Antiparasitic tests were performed as described by Bero *et al*. [40]. *Trypanosoma brucei brucei* (strain 427) bloodstream forms were cultured in vitro in HMI9 medium containing 10 % heat-inactivated foetal bovine serum (Sigma), 150 mM l-cysteine and 20 mM betamercaptoethanol (Sigma-Aldrich, Germany), 0.303 % sodium bicarbonate (Merck), 0.0136 % hypoxanthine (Acros) 0.011 % pyruvate Na (Merck), 38 mg L^{-1} thymidine (Acros) and 28.2 mg L^{-1} bathocuprine disul. (Acros). *Leishmania mexicana mexicana* promastigotes (MHOM/BZ/84/ /BEL46) were cultivated in vitro in HOMEM medium (Thermo-Fisher) supplemented with 0.2 % M199 (Gibco), 0.1 % glucose (Sigma), 0.874 % HEPES Na (Sigma), 0.553 % MOPS Na (Janssen), 0.2 % sodium bicarbonate (Merck), 0.02 % l-alanine (Merck), 0.01% l-arginine (Sigma), 0.007 % l-methionine (Sigma), 0.008 % l-phenylalanine (Acros), 0.06 % l-proline (Acros), 0.016 % Taurine (Acros), 0.006 % l-serine (Sigma), 0.035 % l-threonine

(cc) BY

(Merck), 0.01 % l-tyrosine (Merck), 0.001 % adenosine and guanosine (Serva), 0.005 % d-glucosamine (Calbiochem), 4 mg L^{-1} folic acid (Sigma), 2 mg L^{-1} *p*-aminobenzoic acid (Sigma), 0.2 mg mL^{-1} biotin (Merck), 0.8 % MEM amino acid solution diluted 50 times (Thermo-Fisher), 0.6 % MEM non-essential amino acids diluted 100 times (Thermo-Fisher), 5 µg mL^{-1} of hemin and 15 % heat-inactivated foetal bovine serum (Sigma). *Trypanosoma* cells were incubated in a humidified 5 % CO_2 atmosphere at 37 °C, while *Leishmania promastigotes* were incubated at 28 °C. All tests were performed in a 96-well microplate containing 5×10^4 parasites/well. After 72 hours of incubation, 10 µL of an Alamar Blue solution diluted in PBS solution (1:1) was added. After 4 h of incubation, fluorescence at 5.90 nm was measured with a spectrophotometer (SpectraMax M2e; Molecular Devices, UK). Pentamidine (a commercial antileishmanial drug) and suramine (a commercial antitrypanosomal drug), both from Sigma-Aldrich, were used as positive controls in all experiments with an initial concentration of 1 µg mL^{-1}. First stock solutions of compounds were prepared in DMSO at 20 mg mL^{-1}. The solutions were further diluted in medium to give 0.2 mg mL^{-1} stock solutions. Compounds were tested in eight serial three-fold dilutions (final concentration range: 100-0.05 µg mL^{-1}) in 96-well microtiter plates. All tests were performed at least three times in duplicate. Statistical analyses were conducted using Microsoft Excel software.

Cytotoxicity

Cytotoxic activity of the compounds was assessed by a Cytotoxicity Detection Kit^{PLUS} (LDH) (Roche Diagnostics, Mannheim, Germany) as described previously [23,34,41]. Human monocytic leukaemia THP-1 cell line (European Collection of Cell Cultures, Salisbury, UK) was cultured in RPMI 1640 medium supplemented with 10 % fetal bovine serum (Capricorn Scientific, Ebsdorfergrund, Germany) and an antibiotic solution of 100 U mL^{-1}penicillin and 100 µg mL^{-1}streptomycin (Biosera, Cholet, France). Cells were seeded into 96-well plates (5×10^4 cells *per* well in 100 µL culture medium) and incubated at 37 °C with 5 % CO_2 in the incubator to compound concentrations ranging from 0.1 to 30 µM. Cytotoxic effect was determined after 24 h exposure to the compounds. The maximum concentration of DMSO (Sigma) in the assays never exceeded 0.1 %. Camptothecin (Sigma) was used as a reference drug. The median lethal concentration (LC_{50}) values were determined by generating a concentration-response curve in GraphPad Prism 5.00 [42]. All experiments were conducted in triplicate in three independent experiments.

Metabolic stability using rat or human liver microsomes

The LC-MS method was developed using a Dionex Ultimate 3000SD system (Thermo Scientific), which included a binary high-pressure gradient pump, an autosampler, and a column oven. A Phenomenex C18 Polar column (100×2.1 mm, 2.6 µm) paired with a guard column (Phenomenex C18 Polar, 10×2.1 mm, 2.6 µm) was used for separation and elution. The mobile phase initially consisted of 5 % acetonitrile (A) and 95 % of 0.1% formic acid (B). The gradient was linearly increased to 95 % A and 5 % B over 30 minutes, held for 3 minutes, and then re-equilibrated to the initial conditions for 5 minutes. The flow rate was 0.3 mL min^{-1}, the injection volume was 10 µL, and the column was operated at 23 ± 0.1 °C.

The LC system was coupled to a Bruker MicrOTOF-Q II mass spectrometer (Germany), operating in negative electrospray ionization (ESI) mode. The ionization conditions, optimized by the software, were as follows: capillary voltage, −4000 V; end plate offset, 500 V; source temperature, 220 °C; desolvation gas (nitrogen) flow, 6 L min^{-1}; nebulizer (nitrogen) pressure, 2.0 bar; and collision cell voltage, -10 to 40 eV. The base-peak chromatogram (BPC) was acquired in MS mode by monitoring the *m*/*z* range of 50-1500 with a spectral acquisition time of 1 s. The mass spectrometer was calibrated daily and at the start of each LC run using 10 mM sodium formate in 50 % isopropyl alcohol, with a 20 µL loop flush. This calibration ensured a mass accuracy of <5 ppm across the entire chromatogram. High-resolution mass spectrometry (MS) and

tandem mass spectrometry (MS/MS) spectra were first analysed to determine the elemental formula of each compound. The final identification of target compounds relied on isotope pattern matching with a combination of MS/MS and retention behaviour.

The analysis included the following samples: (1) a blank sample containing the tested molecule (**2c**, c = 20 or 200 μM) incubated with only a NADPH-generating system (B-comp), (2) a blank sample containing rat or human liver microsomes (rat liver microsomes - RLMs or human liver microsomes - HLMs) and a NADPH-generating system (B-RLM or B-HLM) and (3) a sample containing the tested molecule (**2c**) with RLMs and a NADPH-generating system. The incubation times were 40 min.

Metabolite identification was conducted using three independent approaches: 1) A detailed comparison of base peak chromatograms (BPCs) from B-comp, B-RLM, or B-HLM with those of *N*-[3,5-bis(trifluoromethyl)phenyl]-1-hydroxynaphthalene-2-carboxamide (**2c**) sample transformed by RLMs or HLMs; 2) isotope cluster analysis of monoisotopic fluorine-containing compounds, with a maximum 20 % intensity difference between the M and M+1 peaks; and 3) mass defect analysis, where the precise decimal portion (to four significant figures) was searched across the chromatogram with a tolerance of 0.05.

Any peaks found with either approach were examined using a database search, MS/MS search, and metabolic search to determine whether they could be accounted for as possible transformation products of the parental **2c**.

Molecular modelling

Molecular docking simulations were performed to investigate the binding modes of the active compounds against selected protein targets. The crystal structures of *Trypanosoma brucei* trypanothione reductase (TbTR; PDB ID: 6OEZ [43]), *Leishmania mexicana* trypanothione reductase (LmTR; PDB ID: 6I7N [44]), and *Leishmania mexicana* arginase (LmArg; PDB ID: 4IU1 [45]) were utilized.

Molecular docking calculations

Molecular docking simulations were performed to study interactions between the target enzyme and the ligands using AutoDock 4.2 [46]. The protein structures were prepared for docking using the AutoDockTools (ADT) package. Each structure was subsequently subjected to energy minimization (1000 steps of the steepest descent algorithm) using the AMBERff19SB [47] force field in the Amber24 software package [48,49] to relieve steric clashes and optimize the geometry. The 3D structures of ligands **1c** and **4c** were built using PyMOL software [50]. Gasteiger charges were assigned, and non-polar hydrogens were merged using AutoDockTools. The docking calculations were carried out using the Lamarckian Genetic Algorithm (LGA). A grid box was cantered on the active site of the protein. The initial population size was set to 250, the maximum number of energy evaluations to 1×10^7, and the maximum number of generations to 2.7×10^5.

The resulting docking poses were clustered according to their root-mean-square deviation (RMSD) with a tolerance of 2.0 nm. The conformation with the most favourable binding free energy (ΔG) within the most populous cluster was selected for further analysis of protein-ligand interactions.

Molecular dynamics simulations

The most promising docking poses, based on binding energy and cluster occupancy, were selected for refinement through molecular dynamics (MD) simulations using the Amber24 software package [48]. Given the presence of a bimetallic manganese centre in the active site of *Leishmania mexicana* arginase, the MCPB.py [51] tool within the Amber24 package was employed to generate topologies and force field parameters that accurately describe the metal ions and their coordination sphere. The manganese ions were

(cc) BY

treated as +2 cations, and the bonded model was used to define their interactions with the coordinating residues. The protein was described using the all-atom ff19SB force field [47]. The small-molecule inhibitors were parameterized using the General Amber Force Field (GAFF) [52]. Atomic partial charges for the inhibitors were assigned using the AM1-BCC method *via* the antechamber program. Each protein-ligand complex was solvated in a truncated octahedral periodic box of explicit TIP3P water molecules [53], ensuring a minimum distance of 1.00 nm between the solute atoms and the box edges. Sodium ions were added to neutralize the net charge of the system. The system underwent a two-step energy minimization protocol. First, the solvent and ions were minimized with positional restraints (2,092 kJ mol^{-1} nm^{-2}) applied to the solute atoms. Second, the entire system was minimized without any restraints. The minimized systems were then gradually heated from 0 to 300 K over 500 ps in the NVT ensemble (constant number of particles, volume, and temperature), with positional restraints applied to the solute atoms. Subsequently, the systems were equilibrated for 500 ps in the NPT ensemble (constant number of particles, pressure and temperature) at 101.325 kPa (1 atm) to achieve the correct solvent density. Temperature was regulated using a Langevin thermostat with a collision frequency of 1.0 ps^{-1}, and pressure was controlled using a Berendsen barostat. Finally, unrestrained MD simulations were performed for 100 ns for each complex in the NPT ensemble at 300 K and 101.325 kPa. The particle mesh Ewald (PME) method was used to handle long-range electrostatic interactions. A non-bonded interaction cutoff of 0.80 nm was applied, and bonds involving hydrogen atoms were constrained using the SHAKE algorithm, allowing an integration time step of 2 fs. Post-MD analysis was performed using the CPPTRAJ program [54].

Binding free energy calculations using molecular mechanics/generalized born surface area

The relative binding affinities of the protein-ligand (PL) complexes were evaluated using the molecular mechanics/generalized born surface area (MM-GBSA) method [55], following a hierarchical strategy as previously described. This analysis was performed on a set of equidistant snapshots sampled from the final 95 ns of the production trajectories under the single-trajectory approximation.

The binding free energy (ΔG_{bind}) for the association of a ligand (L) with the protein (P) to form the complex (PL) is defined by Equation (1):

$$\Delta G_{bind} = \Delta E_{MM} + \Delta G_{sol} - T\Delta S \quad (1)$$

where ΔE_{MM} represents the gas-phase molecular mechanics energy change, ΔG_{sol} accounts for the solvation free energy and $-T\Delta S$ denotes the contribution of conformational entropy upon binding. The molecular mechanics term, ΔE_{MM}, is composed of internal energy $\Delta E_{internal}$ (including bond, angle and dihedral terms), electrostatic interactions $\Delta E_{electrostatic}$ and van der Waals forces ΔE_{vdW}, Equation (2):

$$\Delta E_{MM} = \Delta E_{internal} + \Delta E_{electrostatic} + \Delta E_{vdW} \quad (2)$$

The solvation term, ΔG_{sol}, is calculated as the sum of polar (ΔG_{PB}) and non-polar (ΔG_{SA}) contributions, Equation (3):

$$\Delta G_{sol} = \Delta G_{PB} + \Delta G_{SA} \quad (3)$$

To further explore the electronic nature of the binding interactions, reduced 3D model systems were constructed based on the representative geometries obtained from the MD trajectories. The selection of residues for these models was guided by the results of the per-residue free energy decomposition (MM-GBSA). Specifically, any residue contributing a binding free energy of $\Delta G > 4.184$ kJ mol^{-1} was identified as a critical component of the binding pocket. The side chains of these key residues, along with the respective inhibitor, were extracted to form the reduced system, thereby enabling high-level quantum-mechanical characterization of the intermolecular contacts within the active site.

Quantum theory of atoms in molecules analysis

To gain deeper insight into the nature of the protein-ligand interactions identified in the docking and MD studies, a quantum theory of atoms in molecules (QTAIM) analysis was performed. This methodology allows the topological characterization of the electron density distribution, $\rho(r)$, within a molecular system.

The topology of $\rho(r)$ is defined by its critical points (CPs), where the gradient of the electron density vanishes ($\nabla\rho(r) = 0$). Critical points are classified by their rank (ω) and signature (σ) as (ω, σ). The key critical point for characterizing chemical interactions is the (3, -1) type, known as the bond critical point (BCP), which is a saddle point in the electron density located between two bonded atoms. The properties of the electron density at the BCP, such as $\rho(r)$ and its Laplacian ($\nabla^2\rho(r)$), provide valuable information about the strength and character (*e.g.* covalent *vs.* non-covalent) of the interaction. For this analysis, the wave functions of the protein-ligand complexes were generated at the M062X/6-31G(d) level of theory. The analysis was focused on the first shell of residues, defined as those having at least one heavy atom within a 0.50 nm radius of the ligand. The QTAIM topology calculations were carried out using the Multiwfn software [56]. This level of theory was selected because it provides an optimal compromise between the accuracy required to obtain reliable electron density derivatives and the computational cost associated with the large size of the systems under study, an approach well established in recent literature [57-61].

Results and discussion

Chemistry

Synthesis

The compounds were prepared by a simple (click chemistry) but innovative microwave synthesis from commercially available building blocks (2-hydroxy-1-naphthoic acid (**1**), 1-hydroxy-2-naphthoic acid (**2**), 4-hydroxyquinoline-3-carboxylic acid (**3**), 4-hydroxy-7-(trifluoromethyl)quinoline-3-carboxylic acid (**4**) and substituted anilines (**a**-**d**)) in anhydrous chlorobenzene in the presence of PCl_3. The synthesis is depicted in Scheme 1 and a list of all studied compounds is given in Table 1.

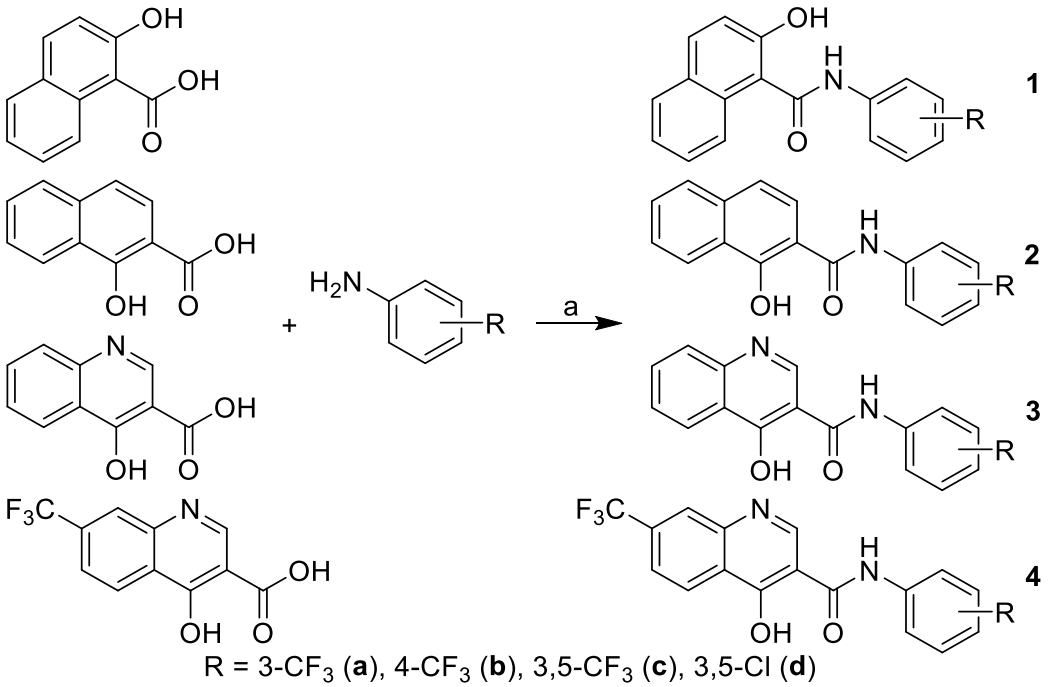

Scheme 1. Synthesis of ring-substituted carboxanilides **1-4d**. Reagents and conditions: (**a**) PCl_3, chlorobenzene, MW, 45 min [23,27,34-36]

(cc) BY

Table 1. Structure of carboxanilides **1a**-**4d**; experimentally determined lipophilicity log *k* values, predicted lipophilicity (log *P*) values, electronic $\sigma_{(Ar)}$ parameters of anilide ring and other parameters of investigated compounds, antileishmanial (Lmm)/antitrypanosomal (Tbb) activity and cytotoxicity on THP-1 cells. IC_{50} and LC_{50} values are expressed as mean ± standard deviation SD.

Comp.	R	MW	log *P*[a]	log *k*	$\sigma_{(Ar)}$[a]	HBD[a]	HBA[a]	RB[a]	TPSA[a], nm^2	Lmm IC_{50}, µM	Tbb IC_{50}, µM	THP-1 LC_{50}, µM
						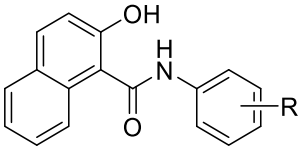						
1a [34]	3-CF_3	331	5.46	0.3287	0.89	2	3	3	0.4933	3.69±0.20	5.24±0.13	>30
1b [34]	4-CF_3	331	5.27	0.3737	0.95	2	3	3	0.4933	4.93±0.36	4.71±0.09	3.3±0.12
1c	3,5-CF_3	399	6.39	0.7844	1.05	2	3	4	0.4933	1.82±0.05	0.561±0.018	>30
1d	3,5-Cl	332	6.09	0.6415	1.11	2	3	2	0.4933	3.55±0.32	2.30±0.10	>30
						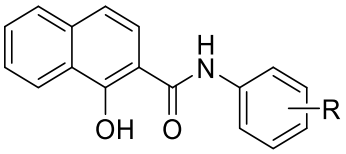						
2a [23]	3-CF_3	331	5.49	0.4931	0.89	2	3	3	0.4933	4.00±0.18	4.27±0.13	1.0±0.11
2b [23]	4-CF_3	331	5.33	0.5606	0.95	2	3	3	0.4933	6.73±0.49	4.54±0.19	0.6±0.25
2c [35]	3,5-CF_3	399	6.51	1.0942	1.05	2	3	4	0.4933	2.33±0.09	1.03±0.04	>30
2d [36]	3,5-Cl	332	6.01	0.9704	1.11	2	3	2	0.4933	2.98±0.14	2.21±0.13	>30
						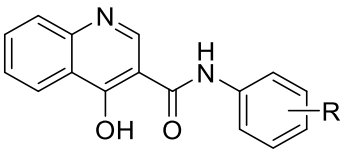						
3a	3-CF_3	332	5.25	0.8211	0.89	2	4	3	0.6222	>150	>150	>30
3b	4-CF_3	332	5.05	0.8672	0.95	2	4	3	0.6222	>301	>301	>30
3c	3,5-CF_3	400	6.39	1.5379	1.05	2	4	4	0.6222	3.74±0.36	4.87±0.16	>30
3d	3,5-Cl	333	5.91	1.2581	1.11	2	4	2	0.6222	3.05±0.15	6.26±0.17	>30
						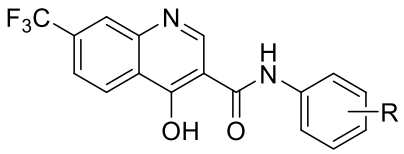						
4a	3-CF_3	400	6.09	0.9728	0.89	2	4	4	0.6222	5.03±0.04	1.86±0.12	>30
4b	4-CF_3	400	5.88	1.0072	0.95	2	4	4	0.6222	9.50±0.97	1.90±0.04	>30
4c	3,5-CF_3	468	6.87	1.9993	1.05	2	4	5	0.6222	7.84±0.29	0.732±0.11	>30
4d	3,5-Cl	401	6.69	1.5097	1.11	2	4	3	0.6222	4.74±0.30	1.33±0.17	>30
Ro5		<500	<5	-	-	<5	<10	-	-	-	-	-
Veber rule		-	-	-	-	-	-	<10	<1.40	-	-	-
PEN		-	-	-	-	-	-			0.054±0.006	-	
SUR		-	-	-	-	-	-			-	0.050±0.005	
CPT		-	-	-	-	-	-	-	-	-	-	0.2±0.07

[a]ACD/Percepta ver. 2025 [62]; MW = molecular weight, HBD = number of H-bond donors, HBA = number of H-bond acceptors, RB = number of rotatable bonds, TPSA = topological polar surface area, PEN = pentamidine, SUR = suramin, CPT = camptothecin, Ro5 = Lipinski's rule of five

X-ray crystallography

Single-crystal X-ray diffraction analysis confirmed the molecular structure of *N*-[3,5-bis(trifluoromethyl)phenyl]-4-hydroxy-7-(trifluoromethyl)quinoline-3-carboxamide (**4c**) (Figure 1). A single crystal of **4c** was prepared by slow evaporation of the acetonitrile solution. The compound crystallizes in the monoclinic crystal system in the space group $P2_1/c$ with four molecules in the unit cell ($Z = 4$). Data were collected at 100 K using Cu Kα radiation ($\lambda = 0.154184$ nm). The crystallographic data and structure refinement parameters are summarized in Table 2.

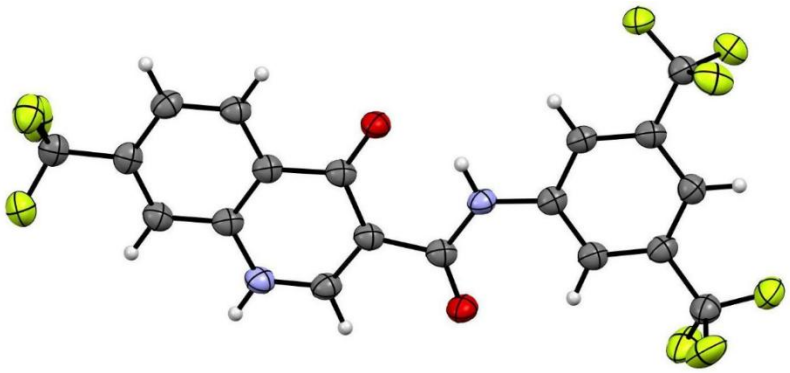

Figure 1. Molecular structure of *N*-[3,5-bis(trifluoromethyl)phenyl]-4-hydroxy-7-(trifluoromethyl)quinoline-3-carboxamide (**4c**) obtained by single-crystal X-ray diffraction (C = grey, O = red, N = blue, F = yellow, H = white)

Table 2. Crystal data and structure refinements for the studied compound **4c**

Formula	$C_{19}H_9F_9N_2O_2$
Formula weight	468.28
Temperature/K	99.98(10)
Crystal system	monoclinic
Space group	$P2_1/c$
a / nm	1.58110 (6)
b / nm	0.650949 (18)
c / nm	1.89382 (7)
α / °	90
β / °	114.495 (4)
γ / °	90
Volume, nm^3	1.77371 (12)
Z	4
D_{calc} / g cm^{-3}	1.754
μ / mm^{-1}	1.612
F(000)	936.0
θ range for data collection, °	6.14-135.95
Reflection collected	9292
Independent reflection	3212
R(int)	0.0344
Data/restrains/parameters	3212/0/289
Goodness-of-fit on F^2	1.056
R_1, wR_2 ($I > 2\sigma(I)$[a]	0.0559, 0.1479
R_1, wR_2 (all data)[a]	0.0632, 0.1577
Largest difference peak and hole, $Å^{-3}$	0.361 and -0.283
CCDC number	2535984

[a] $R_1 = \Sigma(\left|F_o\right| - \left|F_c\right|) / \Sigma\left|F_c\right|$; $wR_2 = [\Sigma w(F_o^2 - F_c^2)^2 / \Sigma w(F_o^2)^2]^{1/2}$

The molecular structure consists of a 7-(trifluoromethyl)quinolin-4-one core bearing a carboxamide substituent at position 3 connected to a 3,5-bis(trifluoromethyl)phenyl group. The crystallographic analysis confirms that the heterocyclic fragment adopts the 4-oxo tautomeric form in the solid state.

Analysis of the molecular geometry shows that the quinolinone core and the 3,5-bis(trifluoromethyl)phenyl ring form a dihedral angle of approximately 6.2°, indicating a nearly planar molecular conformation and efficient conjugation between the two aromatic systems. The amide linker exhibits a torsion angle of C3-C11-N2-C12 = 179.1(2)°, confirming the essentially planar character of the amide group. The molecular conformation is further stabilized by an intramolecular N-H···O and C-H···O hydrogen bonds between the amide nitrogen atom N2 and the hydroxyl oxygen atom O1, and between the aromatic carbon atom C17 and the carbonyl oxygen atom O2, with donor-acceptor distances of 0.2646(2) and 0.2859(3) nm, respectively. The crystal packing of **4c** is further

(cc) BY

stabilized by intermolecular N-H···O hydrogen bonds between the quinolinone nitrogen atom N1 and the carbonyl oxygen atom O2, with the donor-acceptor distance of 0.2838(2) nm, as well as by π-π stacking interaction between the quinolinone core and 3,5-bis(trifluoromethyl)phenyl ring (centroid···centroid distance $C_g \cdots C_g$ = 0.3649 nm), see Figure 2. Structure refinement converged with R_1 = 0.0559 for observed reflections and wR_2 = 0.1577 for all data, indicating a satisfactory structural model.

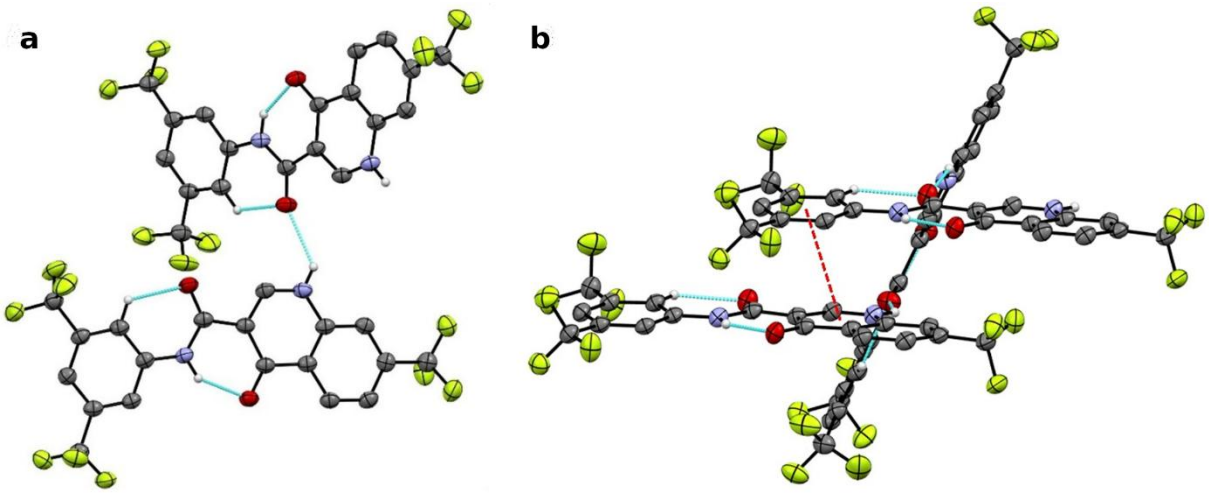

Figure 2. Part of the crystal structure of compound **4c** showing intra- and intermolecular N-H···O and C-H···O hydrogen bonds (blue dashed lines, a) and π-π stacking interactions (red dashed line, b). Hydrogen atoms not involved in these non-covalent contacts are omitted for clarity

Physicochemical and ADME properties

Since the basis for understanding the behaviour of bioactive compounds is the knowledge of their lipo-hydrophilic properties, lipophilicity parameters were determined for all compounds, namely the experimental log *k* (logarithm of the capacity factor; measured by RP-HPLC on a C18 column with methanol as an organic modifier of the mobile phase) and log *P* predicted using the ACD/Percepta ver. 2025 software [62] (Table 1). The log *k* and log *P* values corresponded; for the 4 series with the 4 discussed substances (n = 4), the correlation coefficient r is in the interval 0.94 to 0.98, see Figure 3. Lipophilicity increased in all discussed series in the following order: 3-CF_3 < 4-CF_3 < 3,5-Cl < 3,5-CF_3. Overall, the lipophilicity of both 4-hydroxyquinoline series (4 and 3) was higher than that of the hydroxynaphthalene series, with 2-hydroxynaphthalene-1-carboxamides having the lowest lipophilicity, see Figure 4.

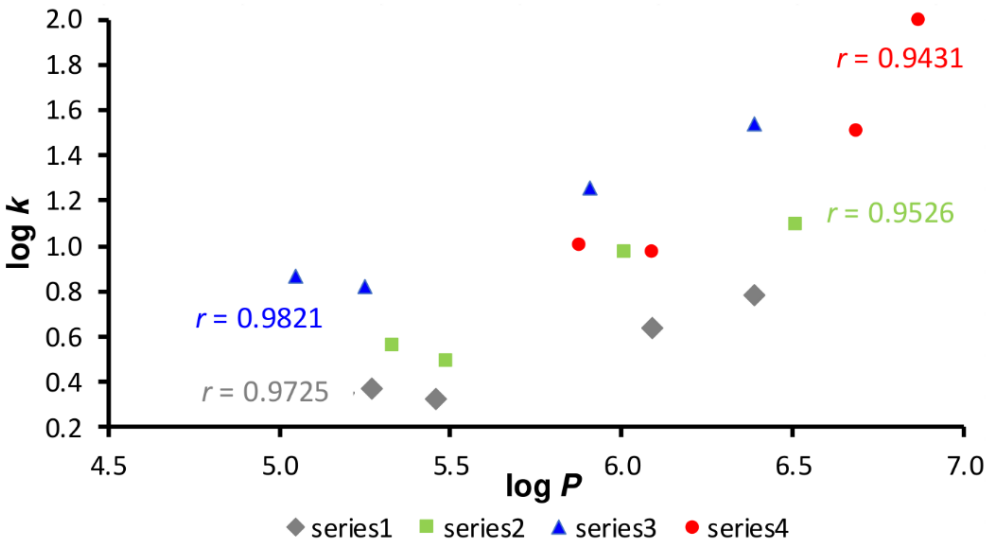

Figure 3. Match of experimentally determined log *k* values with predicted log *P* data using ACD/Percepta of studied compounds **1a-4d**

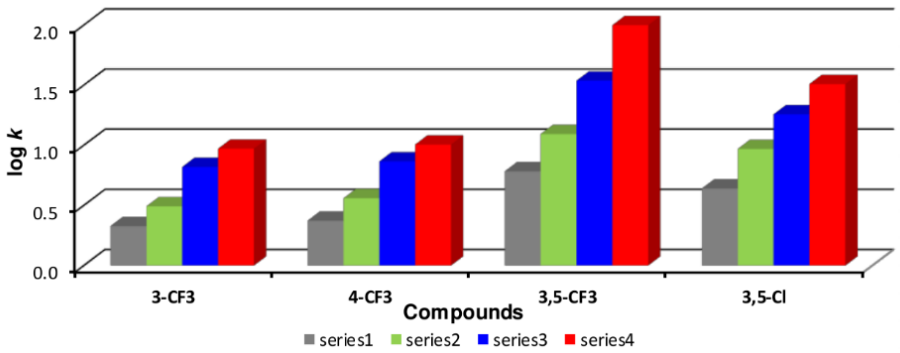

Figure 4. Order of individual derivatives arranged according to increasing log *k* values within individual series

In addition to the lipophilicity, Table 1 also shows the predicted (ACD/Percepta) electronic *σ* parameters of the entire anilide-substituted ring, which characterize the ability of this fragment to donate or withdraw electrons. The σ values range from 0.9 to 1.1.

The gold standard in the design of drug-like molecules is the fulfilment of the criteria of the so-called Lipinski Rule of Five (Ro5) [63], which contains limits of specific molecular descriptors (MW <500, log *P* <5, HBD <5, HBA <10) established on the basis of experimentally and statistically obtained results so that a compound fulfilling this recommendation has a higher chance of becoming a drug. The table also provides recommendations for potential drug molecules based on the Veber Rule [64]. All values were calculated using ACD/Percept. As shown in Table 1, all compounds meet the criteria of Ro5 and the Veber Rule, except for lipophilicity (log P), which is slightly increased and falls within the log *P* interval of 5.05-6.87. It is important to note that a good drug-like score does not make a molecule a drug, and vice versa [65-67]. Approved drugs with log *P* <5 since 2000 represent a trend between 10 to 15 % [68], and potentially more problematic bioavailability can be addressed by formulation strategies [68,69].

Bioassays

The compounds were selected to meet the definition of Michael acceptors [30,70]; thus, based on previous studies [29,30,33], significant activity is expected. The substances were evaluated against the promastigotes of *Leishmania mexicana mexicana* (Lmm) MHOM/BZ/84/BEL46 and the bloodstream form of *Trypanosoma brucei brucei* (Tbb) strain 427; the activity was expressed as IC_{50}. The cytotoxicity of the studied compounds, expressed as LC_{50} values, was determined in the human monocytic leukaemia cell line THP-1. Only three derivatives (1b, 2a, 2b) showed cytotoxic activity; their LC_{50} values ranged from 3.3 to 0.6 µM. The other compounds induced no cytotoxic effects up to the highest concentration evaluated of 30 µM. All biological screening results are shown in Table 1.

Overall, the most effective compound against both protozoa was *N*-[3,5-bis(trifluoromethyl)phenyl]-2-hydroxynaphthalene-1-carboxamide (**1c**) with an IC_{50} of 0.56 µM against Tbb and 1.82 µM against Lmm. Other active derivatives against both pathogens were *N*-[3,5-bis(trifluoromethyl)phenyl]-1-hydroxynaphthalene-2--carboxamide (**2c**) and *N*-(3,5-dichlorophenyl)-1-hydroxynaphthalene-2-carboxamide (**2d**), with IC50 values of 1.03 and 2.21 µM against Tbb, and 2.33 and 2.98 µM against Lmm, respectively. Compound **1d** also showed very good activity against both tested protozoa. Among the tested compounds, *N*-[3,5-bis(trifluoromethyl)phenyl]-4-hydroxy-7-(trifluoromethyl)quinoline-3-carboxamide (**4c**) also showed high selective activity against Tbb (IC_{50}= 0.73 µM).

Derivatives **3a** and **3b** were the least active against both Tbb and Lmm. Overall, the compounds showed similar activity against Tbb and Lmm, although series 4 showed the best activity against Tbb, while series **1**

(cc) BY

and **2** showed the highest activity against Lmm. At the same time, monosubstituted derivatives **a**/**b** (3-CF_3 and 4-CF_3) from all series had worse activity than disubstituted derivatives **c**/**d** (3,5-CF_3 and 3,5-Cl). We can therefore speak of the advantages of substitution with more electron-withdrawing substituents ($\sigma > 1$) and in the case of activity against Tbb, we can also speculate about the positive effect of higher lipophilicity, as described by Kos *et al*. [29].

In addition to the antiparasitic evaluation, the metabolic stability of compound **2c**, selected as one of the most active derivatives identified in the biological screening, was assessed using rat liver microsomes (RLMs) and human liver microsomes (HLMs). Under the experimental conditions, **2c** showed no detectable metabolic transformation. No metabolites attributable to this compound were identified by any of the three analytical approaches employed, namely difference base-peak chromatograms, isotope cluster analysis, and mass defect analysis, following a 20 min incubation at concentrations of 20 and 200 µM. The absence of detectable biotransformation products indicates high metabolic stability in both microsomal systems. These findings complement the favourable antiparasitic activity of **2c** and further support its potential for future development.

Overall, the biological evaluation revealed distinct activity trends across the investigated scaffolds and substitution patterns, indicating that relatively small structural modifications markedly influence antiparasitic potency. These observations provided the basis for subsequent molecular modelling studies aimed at rationalizing the experimentally observed structure-activity relationships.

Molecular modelling - searching for potential molecular targets

While the compounds demonstrated potent activity against the parasites, their precise molecular targets remain unknown. To generate testable hypotheses regarding their potential mechanisms of action, we employed a computational target-driven approach.

Based on an extensive database search, we selected several essential enzymes from each parasite's metabolism as putative molecular targets. This selection was guided primarily by the chemical nature of our compounds and their similarity to previously reported inhibitor scaffolds, namely trypanothione reductase (TR) for *Trypanosoma brucei*, and both TR and arginase for *Leishmania mexicana*. In addition to the structural features of the ligands, the selection of these targets is supported by their critical biological roles and parasite-specific nature, as none of them has a functional human homologue [71-74], enabling the design of selective inhibitors with minimal expected host toxicity. Moreover, these enzymes are essential for parasite survival [72,73,75], as they participate in key metabolic and redox homeostasis pathways [43,72,73,76,77], making their inhibition likely to severely compromise parasite viability.

Trypanothione reductase is a particularly attractive molecular target due to its conservation among kinetoplastid parasites, including Trypanosoma brucei and Leishmania mexicana, thereby enabling the exploration of dual inhibitors with potential activity against multiple neglected tropical diseases [43,72,73,77]. From a computational standpoint, the selected targets are well suited for high-precision *in silico* characterization. TR from *L. mexicana* (PDB ID: 6I7N [44]) and *T. brucei* (PDB ID: 6OEZ [43]) exhibited favourable docking scores and strong binding affinities toward the lead compounds. In the case of L. *mexicana* arginase (PDB ID: 4IU1 [45]), reliable modelling required special attention due to its binuclear Mn^{2+} active site. This was successfully addressed through metal coordination parametrization using the MCPB.py tool [51].

Using these prepared structures, we subsequently performed molecular docking, molecular dynamics simulations and quantum theory of atoms in molecules (QTAIM) calculations to evaluate the structural feasibility and binding modes of the lead compounds (**1c** and **4c**). In addition, the same computational protocol was applied to known reference inhibitors for each target protein, namely H6H for *L. mexicana* TR [44], NNH

for *L. mexicana* arginase [45], and M9J for *T. brucei* TR [43], enabling a consistent comparative analysis. Figure 5 schematically summarizes the computational workflow and presents the chemical structures of the reference inhibitors used for each target.

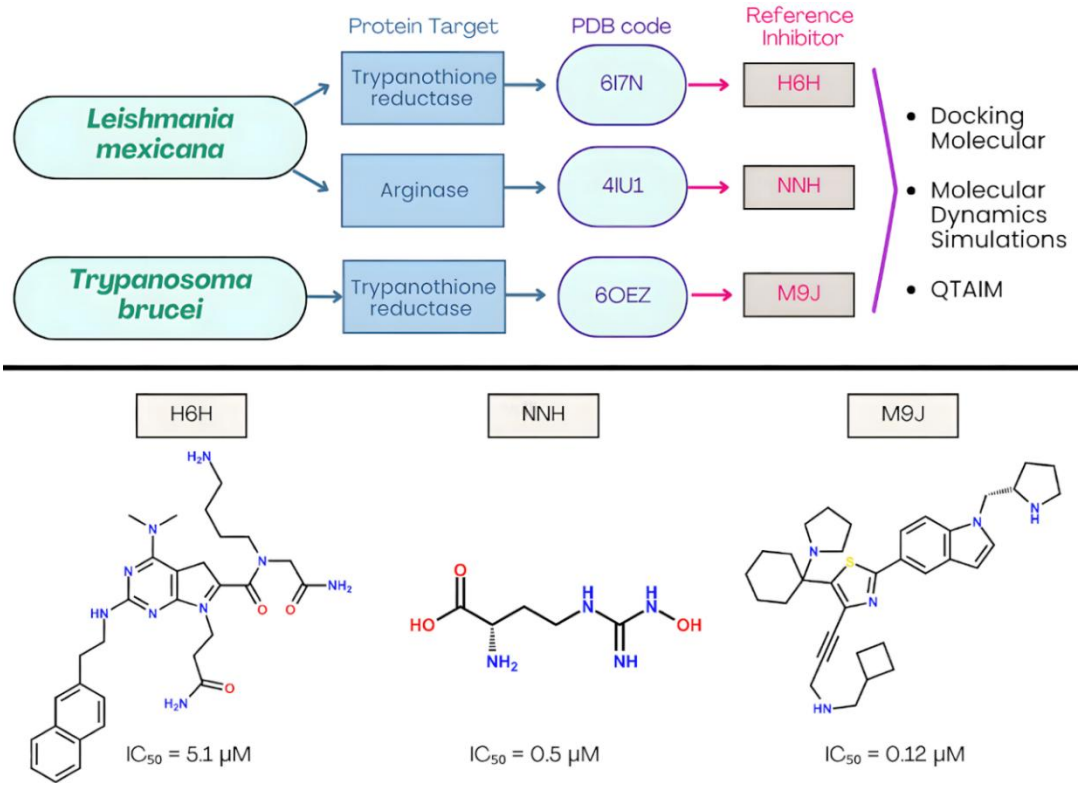

Figure 5. Overview of the computational workflow and reference inhibitors for *Leishmania mexicana* and *Trypanosoma brucei* targets. The upper panel illustrates the integrated strategy, including protein target selection (trypanothione reductase and arginase), corresponding PDB structures (6I7N, 4IU1, 6OEZ), and the sequential application of molecular docking, Molecular Dynamics simulations, and QTAIM analysis. The lower panel displays the chemical structures and experimental IC_{50} values of the reference inhibitors used in this study

Leishmania mexicana

As described in the previous section, we performed molecular simulations for two potential molecular targets of this parasite: i) *Leishmania mexicana* TR and ii) arginase. These targets were selected based on the structural similarity between the compounds reported here and the known inhibitors H6H for TR and NNH for arginase. Molecular modelling studies were performed using a combination of techniques: docking calculations, followed by molecular dynamics simulations, and QTAIM calculations (see details in the methods section).

Trypanothione reductase

The target protein for this study was trypanothione reductase. Given the lack of crystal structures for *Leishmania mexicana* TR, the structural model was based on the homologous enzyme from *Leishmania infantum*, which shares a 91 % sequence identity in the catalytic site. The crystal structure (PDB ID: 6I7N; co-crystallized with inhibitors H6H and FAD, resolved as a dimer at 0.33 nm) was selected as the template. While the structure 6I7N is a dimer, its complete assembly was retained for subsequent simulations. Other available structures were reviewed, but 6I7N was chosen for its optimal resolution and presence of relevant ligands [75,77-79].

To determine the initial binding conformation of compound **1c** (active against *Leishmania*) and the control compound H6H, molecular docking studies were performed using the AutoDock program. In addition, the binding positions were validated using the Neurosnap-Boltz 2 platform (AlphaFold3) [80]. Both methods showed consistent agreement regarding the orientation and location of the ligands within the homodimeric active site (see Figure 6).

(cc) BY

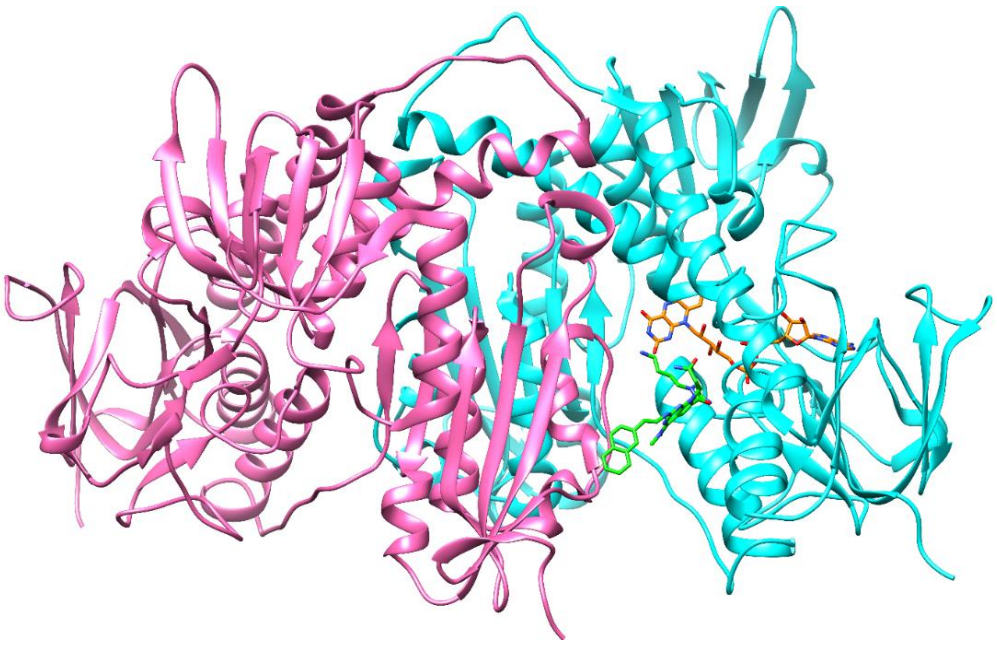

Figure 6. Homodimeric assembly of the TR of *Leishmania mexicana* where one monomer is shown in pink and the other in cyan. In this figure, the bound inhibitor H6H is highlighted in green and the FAD cofactor in orange

In the next step, MD simulations were performed in triplicate for compound **1c** and the reference inhibitor H6H. Each simulation was extended to 100 ns, resulting in an aggregated simulation time of 300 ns per system. The equilibrated trajectories were subsequently subjected to molecular mechanics/Poisson-Boltzmann surface area (MM-PBSA) calculations to estimate and compare the binding free energies of **1c** and H6H. Compound **1c** exhibited a mean binding free energy (ΔG_{bind}) of approximately -66.48 kJ mol^{-1}, which was comparable to that obtained for the reference inhibitor H6H -109.91 kJ mol^{-1}. Interaction analysis revealed that both ligands engage a conserved network of key residues within the binding site, including N402, R472, W21, S109, and M113. Importantly, the high degree of overlap observed in the residue-level interaction profiles, together with similar MM-PBSA binding free energies, indicates comparable binding modes and supports 1c's ability to effectively mimic the binding behaviour of the reference inhibitor (see Figure 7).

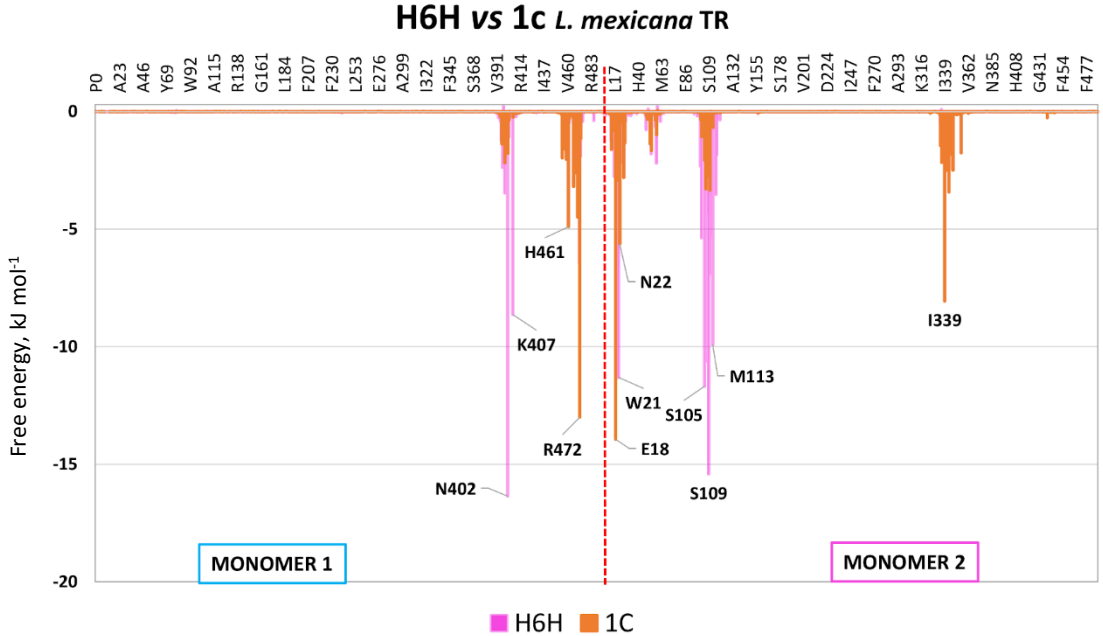

Figure 7. Overlaid histograms of MM-PBSA interaction energies for compounds H6H (magenta) and **1c** (orange) with the main residues involved in complex formation. Contributions from each monomer of the homodimeric protein are displayed in cyan and pink, respectively, and are separated by a red dashed line

To further characterize the most representative binding mode, a clustering analysis was performed on the last 95 ns of each MD trajectory to identify a representative structure for each complex. QTAIM analyses were subsequently performed on these representative structures to evaluate and compare the key intermolecular interactions. As illustrated in Figure 8, QTAIM analysis revealed a conserved network of stabilizing interactions between both ligands and key residues within the active site. For the reference inhibitor H6H, significant electron density contributions were observed for interactions involving residues W21, I106, S109, M113, and D116. In the case of compound **1c**, a comparable interaction pattern was identified, including key contacts with residues E18, W21, N22, T26, V346, E347, and R472', highlighting the engagement of conserved binding determinants across both systems.

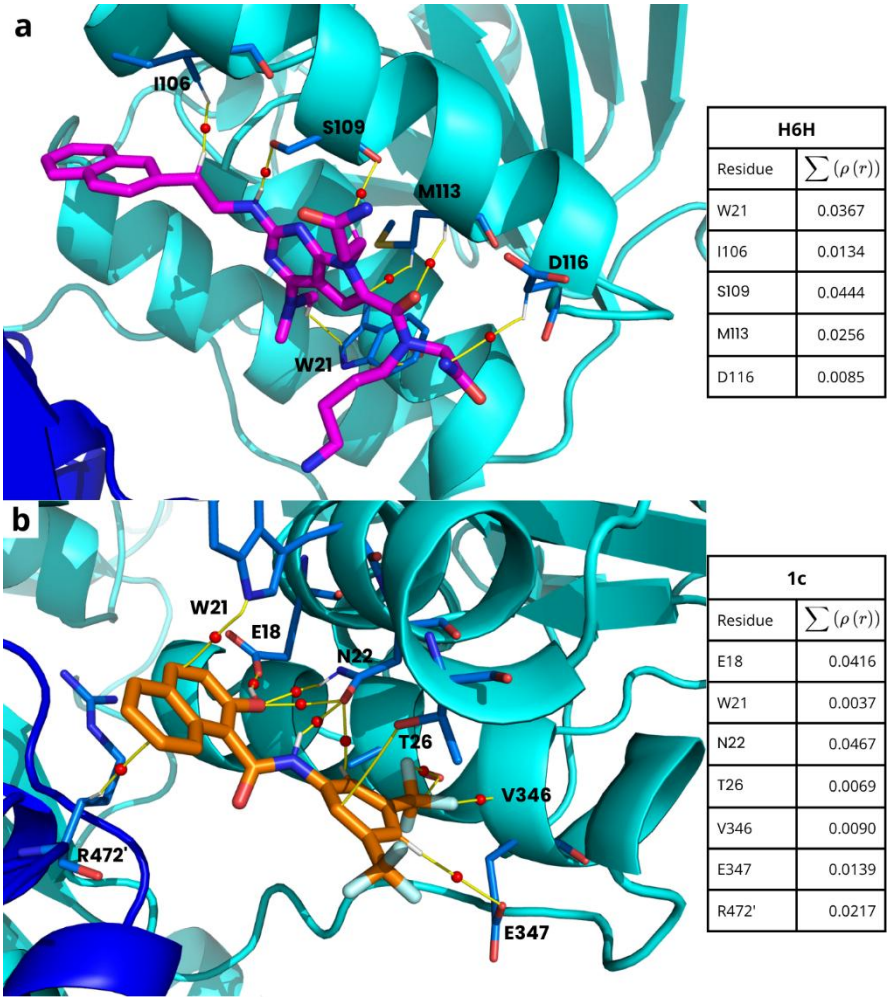

H6H	
Residue	$\sum(\rho(r))$
W21	0.0367
I106	0.0134
S109	0.0444
M113	0.0256
D116	0.0085

1c	
Residue	$\sum(\rho(r))$
E18	0.0416
W21	0.0037
N22	0.0467
T26	0.0069
V346	0.0090
E347	0.0139
R472'	0.0217

Figure 8. QTAIM topological analysis of the interaction networks within the *L. mexicana* TR binding site. a) Molecular graph of charge density obtained for the homodimeric enzyme in complex with the reference inhibitor H6H (in magenta). b) Molecular graph obtained for the complex with compound **1c** (in orange). Yellow lines connecting the nuclei represent the bond paths, while the small red spheres along these paths indicate the bond critical points (BCPs). Adjacent to each molecular graph, a table displays the electron density (ρ) values calculated for the most significant residues involved in ligand stabilization for each case

The total electron density (ρ) values were 0.1613 a.u. for H6H and 0.1629 a.u. for compound **1c**, indicating a highly similar interaction strength and nature for both complexes. The residue-specific interaction profiles shown in Figure 8 further support this similarity, as both ligands establish strong stabilizing contacts with residues located in equivalent regions of the binding site. Notably, the involvement of key residues such as W21, S109, and R472' underscores the structural and energetic equivalence of the two binding modes.

The integration of MM-PBSA energetic landscapes and QTAIM topological analysis provide robust evidence for the binding efficacy of compound **1c** against *Leishmania mexicana* TR. A primary conclusion of

(cc) BY

this study is that **1c** serves as a high-fidelity structural mimic of the co-crystallized inhibitor H6H, achieving a nearly identical total electron density (ρ_{total} ≈ 0.16 a.u.) and a comparable energetic profile. The binding mechanism is defined by a shared reliance on a conserved network of key residues within the active site. While the reference inhibitor H6H exhibits deeper energetic wells at specific residues such as N402 and S109 (reaching approximately -15.89 kJ mol^{-1}), compound **1c** compensates through robust interactions with R472 (-12.97 kJ mol^{-1}) and a more distributed stabilization across residues E18, N22, and I339. Furthermore, the analysis confirms the essential role of the dimeric assembly, as both inhibitors effectively bridge the two subunits of the enzyme. This is evidenced by significant electron density and energetic contributions from R472/R472', which acts as a conserved structural anchor across both systems. The QTAIM results further reveal that **1c** (ρ = 0.1629 a.u.) slightly exceeds the total intermolecular electron density of H6H (ρ = 0.1613 a.u.), suggesting that the synthetic derivative effectively captures the quantum-mechanical determinants required for stable complex formation within the *Leishmania* active site. In summary, the high degree of overlap in the residue-level interaction profiles and the convergence of classical and quantum-mechanical descriptors support the role of **1c** as a potent TR inhibitor, suggesting that targeting the conserved W21-S109-R472 triad is a viable strategy for developing novel leishmanicidal agents.

Leishmania mexicana arginase

Molecular docking was first employed to generate initial binding poses for the compounds. The most promising geometries, identified by docking scores and visual inspection, were then used as starting points for molecular dynamics simulations to refine the interactions and assess complex stability. A per-residue energy decomposition analysis was conducted to elucidate the distinct binding mechanisms of the crystallized reference inhibitor, NOR-*N*-ω-hydroxy-l-arginine (NNH), and the novel synthetic compound **1c** reported here, and to rationalize the experimental inhibitory activity (IC_{50}) observed for both compounds. In our analysis, we focused on key non-covalent interactions within the active site and considered interactions with both Mn atoms. However, we explicitly excluded residues involved in direct coordination with the catalytic manganese ions (Mn^{2+}) (D101, H102, S103, V124, D125, A126, H127, A128, D129, I130, Y230, D231, V232, D233 and T234), as their overwhelmingly favourable coordination energies would dominate the analysis and obscure the subtler interactions governing ligand specificity and affinity.

The energy decomposition profiles shown in Figure 9 reveal two fundamentally distinct modes of binding. The crystallized reference inhibitor (NNH) exhibits a metal-dependent binding mechanism. Its non-covalent interactions with the active site residues are uniformly weak: V137 (ΔG = - 2.59 kJ mol^{-1}), S138 (ΔG = = - 3.97 kJ mol^{-1}), H142 (ΔG = -4.47 kJ mol^{-1}), D182 (ΔG = -1.08 kJ mol^{-1}), E185 (ΔG = -0.25 kJ mol^{-1}) and T245 (ΔG = -1.58 kJ mol^{-1}). In stark contrast, its interactions with the catalytic manganese ions are overwhelmingly favourable (Mn1: -76.31 kJ mol^{-1}; Mn2: -43.51 kJ mol^{-1}). This indicates that its exceptional affinity and lower IC_{50} could be almost entirely driven by strong, specific coordination interactions with the bimetallic centre, which is consistent with its role as a substrate analogue that directly engages the core catalytic machinery. Conversely, compound **1c** could employ a hybrid binding strategy. It maintains a very strong interaction with one manganese ion (Mn1: ΔG = -92.51 kJ mol^{-1}) but shows a slightly destabilizing interaction with the other (Mn2: ΔG = 3.09 kJ mol^{-1}). This trade-off allows it to engage the protein scaffold much more effectively than the reference inhibitor. It forms a broad, strong, and balanced non-covalent network with key residues: H142 (ΔG = -14.77 kJ mol^{-1}), V137 (ΔG = -6.61 kJ mol^{-1}), T245 (ΔG = -6.52 kJ mol^{-1}), S138 (ΔG = -5.69 kJ mol^{-1}), E185 (ΔG = -4.94 kJ mol^{-1}) and D182 (ΔG = = -4.60 kJ mol^{-1}). This demonstrates that **1c** could achieve its significant binding affinity through a powerful synergistic effect combining a potent anchor to one metal ion with a multitude of strong van der Waals, hydrophobic, and electrostatic interactions distributed across the active site. This analysis provides a clear rationale for the found experimental bioactivity. The crystallized inhibitor's

superior potency is predicated on its optimal bidentate coordination with both manganese ions. Compound **1c**, while slightly less potent, achieves its affinity through a more diversified mechanism. This hybrid binding mode optimizing both metal coordination and extensive non-covalent contacts, is highly advantageous. It may confer greater selectivity and reduced susceptibility to resistance mutations that specifically target the metal-coordination site, because the inhibitor's binding does not rely solely on it. The profile of **1c** could be exceptionally promising, demonstrating a successful design strategy that more comprehensively leverages the active-site environment and provides a strong foundation for further structural optimization.

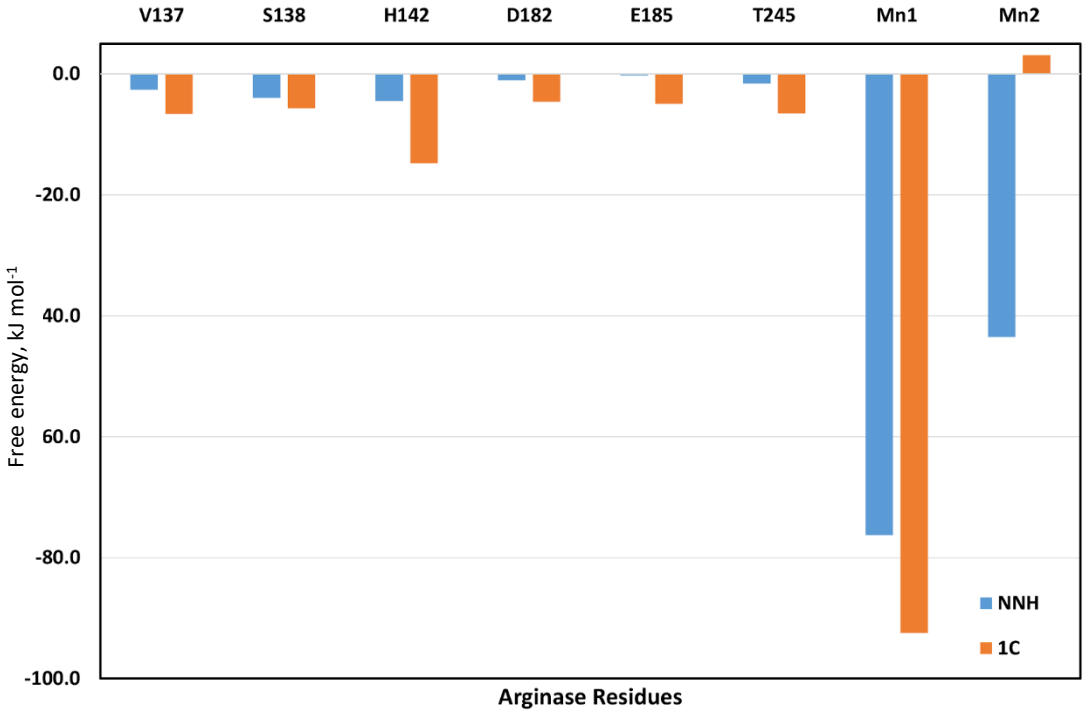

Figure 9. Per-residue decomposition of interaction energies from MM/PBSA calculations. The histogram shows the contribution of individual arginase residues to the total binding energy, with blue and orange bars representing the NNH and **1c** compounds, respectively

While the MM-PBSA analysis provided energetic insights, to further characterize the nature and strength of the non-covalent interactions at an electronic level, a QTAIM analysis was performed. This method provides a rigorous quantum-mechanical description of chemical bonding by analysing the electron density distribution, $\rho(r)$, at the bond critical points (BCPs) corresponding to intermolecular interactions. Unlike the MM-PBSA energy decomposition, this analysis includes all residues that participate in non-covalent interactions, providing a complete topological map of the binding interface. The QTAIM analysis for the reference inhibitor NNH confirms its binding mode is dominated by coordination to the manganese ions. This is evidenced by the very high electron density values at the BCPs corresponding to the Mn-ligand interactions (Mn1: $\rho(r)$ = 0.197 a.u.; Mn2: $\rho(r)$ = 0.118 a.u.). Beyond the metal centre, the analysis reveals a network of weaker, primarily electrostatic interactions. The most significant non-covalent contacts are with S138 ($\sum\rho(r)$ = 0.049), T245 ($\sum\rho(r)$ = 0.049) H142 ($\sum\rho(r)$ = 0.070) and N140 ($\sum\rho(r)$ = 0.041). The main interactions stabilizing the complexes are shown in Figure 10 from molecular graphs.

The cumulative electron density for these residues indicates a binding mode in which strong metal coordination is supplemented by a specific shell of hydrogen-bonding interactions. In stark contrast, the QTAIM topology for compound **1c** reveals a binding profile completely devoid of direct coordination to the manganese ions ($\rho(r)$ = 0 at both Mn1 and Mn2), unequivocally confirming its status as a pure non-covalent inhibitor. Instead, the interaction network is characterized by a set of strong, well-defined interactions with

(cc) BY

residues other than NNH. The most critical interaction is with D182, which shows the highest electron density value (∑ρ(r) = 0.024), suggesting the formation of a very strong hydrogen bond that serves as a primary anchor. Significant interactions are also observed with E185 (∑$\rho(r)$ = 0.013), N140 (∑$\rho(r)$ = 0.007) and H142 (∑$\rho(r)$ = 0.009). The main interactions that stabilize the complex of compound 1 at the active site of *Leishmania mexicana* arginase can be observed in more detail in the molecular graph shown in the supporting section (Figure S41). The molecular graph obtained for NHN, the reference compound for comparison, is also shown in the same figure.

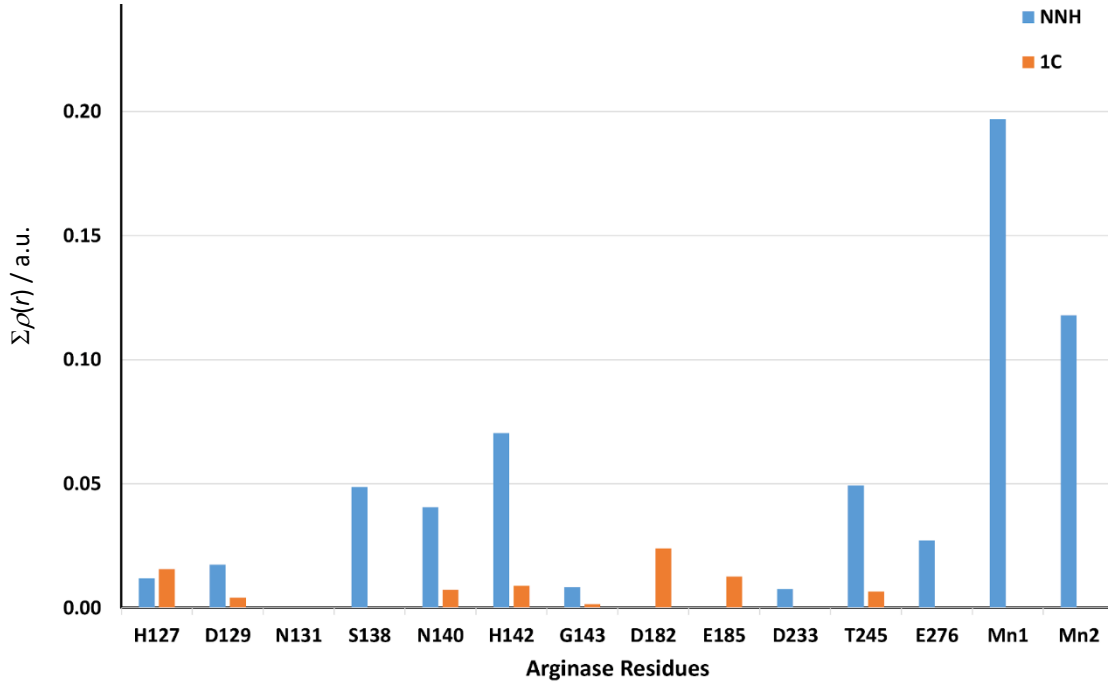

Figure 10. Bar chart comparing the sum of the electron density values, $\rho(r)$, at the bond critical points (BCPs) for intermolecular interactions. The blue bars represent interactions between arginase residues and the NNH ligand, while the orange bars correspond to interactions with the **1c** compound.

In summary, MD studies combined with QTAIM calculations suggest that the two inhibitors could bind to the enzyme through two fundamentally distinct mechanisms. In the case of the NNH compound, its binding is dependent on coordination to the manganese ions, a finding supported by both highly favourable decomposition energies and elevated electron density ($\rho(r)$) values at the bond critical points (BCPs) of the metals. This predominant interaction is complemented by a network of hydrogen bonds with cavity residues. In contrast, compound **1c** exhibits a purely non-covalent binding mechanism, confirmed by the complete absence of electron density at the BCPs of the manganese ions. Instead, its binding mechanism relies on an extensive network of strong electrostatic interactions and hydrogen bonds with key residues such as D182 and E185, defining a unique and highly specific binding profile.

Trypanosoma brucei

The target enzyme used for this study was TR from *Trypanosoma brucei*. The structural models were derived from the crystal structures deposited under PDB IDs: 6OEZ, 6OEX, and 6OEY. These structures, determined by X-ray diffraction at 0.250 nm resolution, represent the enzyme as a homodimer complexed with the FAD cofactor and the inhibitor M9J (Figure 11).

Molecular docking simulations were conducted using the AutoDock software. The binding affinities of the potent compounds **1c** (IC_{50}=0.561±0.018 µM) and **4c** (IC_{50}=0.732±0.11 µM) were evaluated, utilizing M9J (IC_{50}=0.120 µM) as the reference ligand.

MD simulations were then performed to refine the docking-derived binding poses and evaluate the structural stability of the enzyme-ligand complexes. For the production phase, 100 ns trajectories were run in triplicate for the M9J, 1c, and 4c complexes within the *T. brucei* TR dimer, providing a cumulative sampling of 300 ns per system to ensure structural convergence. To further dissect the energetic basis of these interactions, an MM-PBSA free energy decomposition was performed over the final 95 ns of each trajectory.

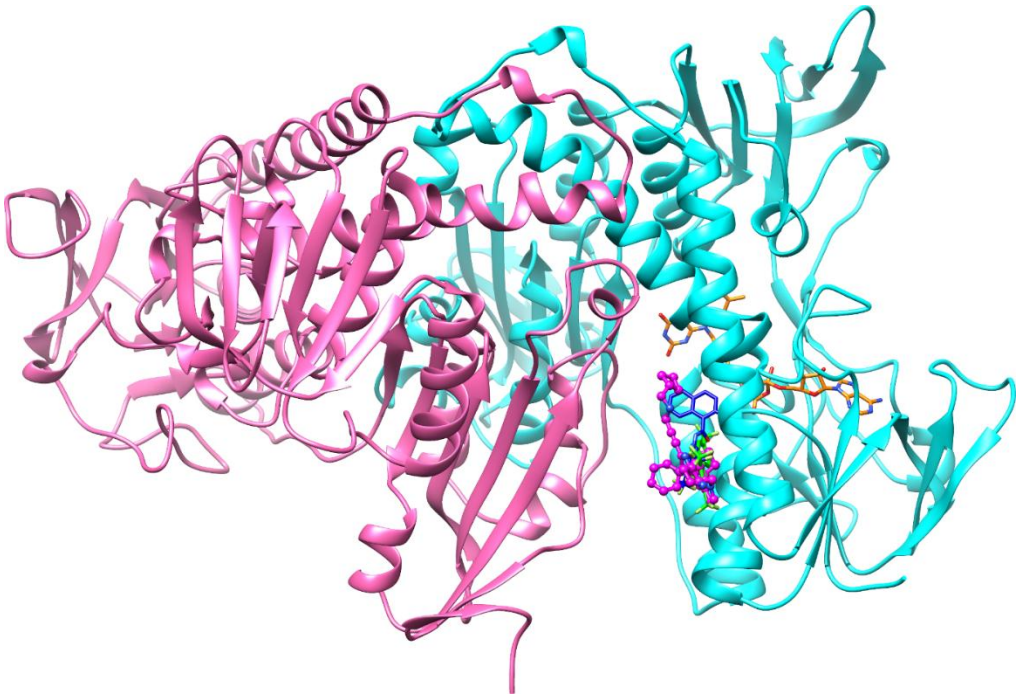

Figure 11. Structural representation of the *T. brucei* TR homodimer. The protein is shown in its dimeric assembly, with monomers coloured in pink and cyan. The binding orientations of the inhibitors are highlighted: M9J (magenta), **1c** (blue), and **4c** (green). The FAD cofactor is represented in orange

This analysis allowed for the identification of key residue-wise contributions to the total binding affinity. The binding energy profile for M9J is predominantly characterized by interactions within Monomer 1, with major energetic contributions from residues L17, W21, Y110, and M113, while R472 from Monomer 2 provides a significant stabilizing effect, reinforcing the critical role of the dimeric interface in ligand recognition and stability (Figure 12a). Similarly, compound **1c** maintains a binding footprint similar to the reference compound, with the most prominent interactions involving L17, G49, Y110, and I339 within Monomer 1, alongside the conserved energetic contribution of R472 from Monomer 2, suggesting a consistent binding mode across these scaffolds (Figure 12b). In contrast, compound **4c** exhibits a distinct and significantly enhanced binding profile dominated by a robust contribution from E18 (ΔG approx. -46 kJ mol^{-1}) followed by W21. Despite these shifts within Monomer 1, the contribution of R472 from Monomer 2 remains a constant structural anchor, highlighting its essential role in stabilizing the complex across different ligands (Figure 12c).

Once again, QTAIM analysis was performed on a reduced system, derived from a clustering analysis of the final 95 ns of the dynamic trajectories. This analysis compared the nature and strength of the intermolecular interactions for compounds M9J, **1c** and **4c**. The total intermolecular electron density (ρ_{total}) followed the trend: **1c** (0.2799 a.u.) > M9J (0.1830 a.u.) > **4c** (0.1736 a.u.). Despite the superior ρ_{total} values exhibited by **1c**, which point toward a highly robust intermolecular network, this electronic advantage did not translate into higher inhibitory potency. In fact, **1c** showed a significantly higher IC_{50} = 0.561 μM compared to the reference M9J (IC_{50} = 0.120 μM). This discrepancy suggests that while the local quantum interactions in **1c** are strong, other factors, such as desolvation penalties or conformational entropy, might influence the overall macro-affinity.

(cc) BY

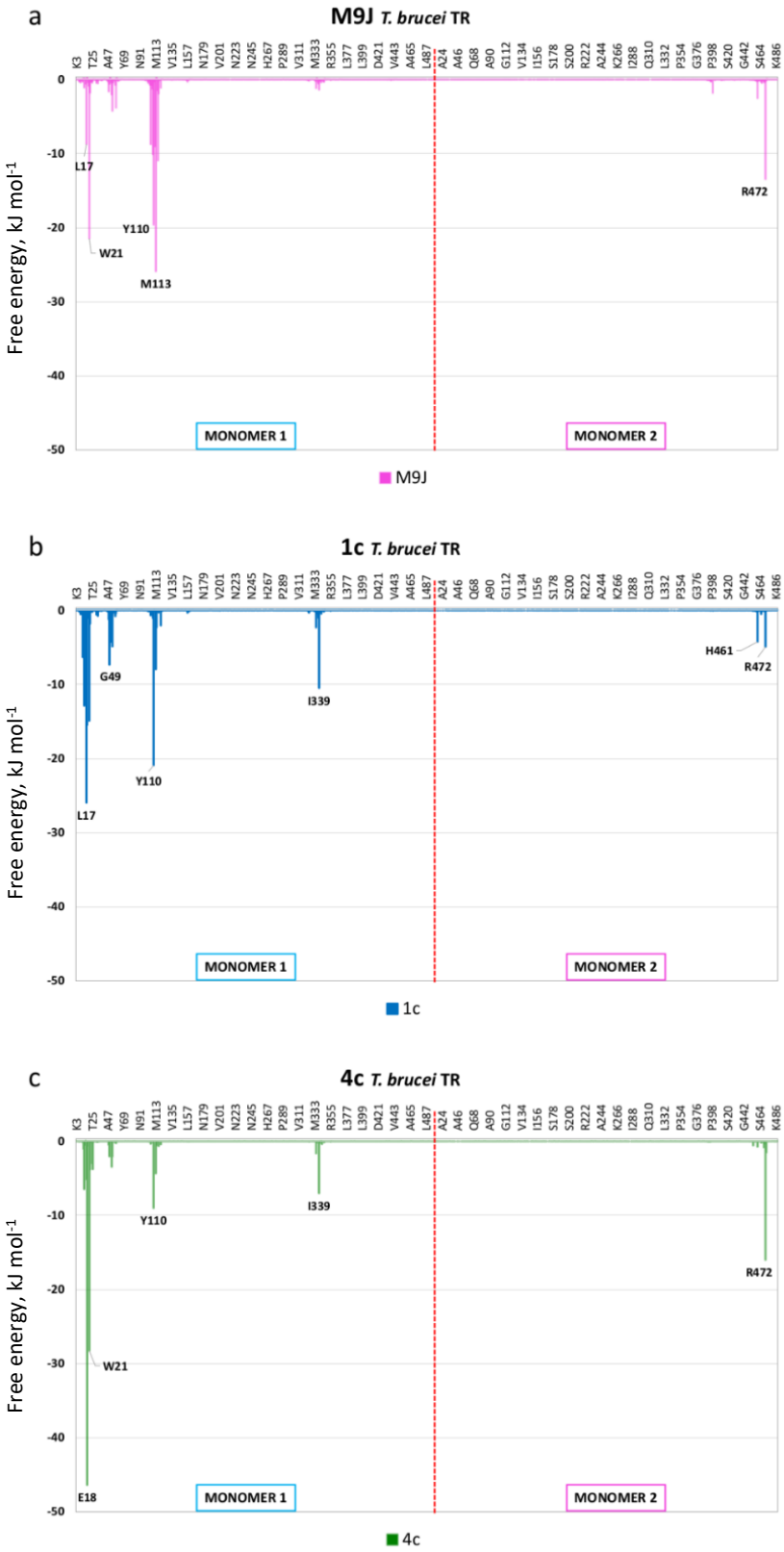

Figure 12. Histograms of MM-PBSA interaction energies for compounds (a) M9J, (b) **1c** and (c) **4c** with the main residues involved in complex formation. Contributions from each monomer of the homodimeric protein are displayed in cyan and pink, respectively, and are separated by a red dashed line

Furthermore, the distribution of the electronic density appears to be as critical as its magnitude; while **1c** exhibits high local ρ values, M9J displays a more balanced and synergistic interaction network across the entire binding pocket. This suggests that for *T. brucei* TR, achieving an optimal fit that minimizes structural strain may be more beneficial for inhibitory potency than maximizing the strength of specific, isolated contacts.

Consequently, these results highlight that QTAIM descriptors should be integrated with macroscopic thermodynamic data to fully rationalize the structure-activity relationships in this dimeric target.

The *per*-residue decomposition of ρ values, as detailed in the tables included in Figure 13, highlights the distinct binding signatures of the studied compounds. M9J exhibits a highly distributed interaction pattern, where its superior inhibitory activity is supported by significant electronic contributions from Y110 (0.0496 a.u.) and W21 (0.0246 a.u.). These residues appear optimally positioned for stabilization within the reference complex. Notably, this high electron density directly correlates with the major free energy contributions identified in the MM-PBSA decomposition, suggesting that the potency of the reference compound is rooted in an energetically and electronically optimized placement within Monomer 1.

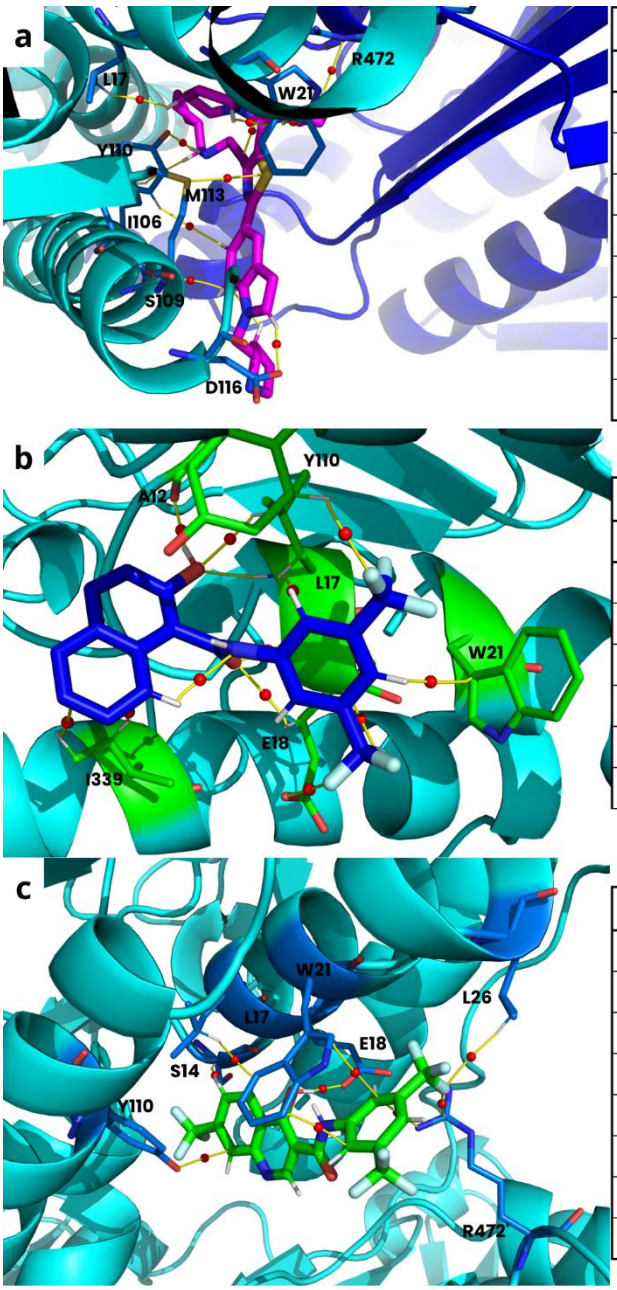

M9J	
Residue	$\sum(\rho(r))$
L17	0.0141
W21	0.0246
I106	0.0111
S109	0.0032
Y110	0.0496
M113	0.0210
D116	0.0239
R472	0.0150

1c	
Residue	$\sum(\rho(r))$
A12	0.0439
L17	0.0455
E18	0.0507
W21	0.0143
Y110	0.0084
I339	0.0133

4c	
Residue	$\sum(\rho(r))$
S14	0.0200
L17	0.0139
E18	0.0717
W21	0.0162
L26	0.0078
Y110	0.0024
R472'	0.0078

Figure 13. QTAIM topological analysis of the interaction networks within the *T. brucei* TR binding site. a) Molecular graph of charge density obtained for the homodimeric enzyme in complex with the reference inhibitor M9J (in magenta). b) Molecular graph obtained for the complex with compound **1c** (in blue). c) Molecular graph obtained for the complex with compound **4c** (in green). Yellow lines connecting the nuclei represent the bond paths, while the small red spheres along these paths indicate the bond critical points (BCPs). Adjacent to each molecular graph, a table displays the electron density (ρ) values calculated for the most significant residues involved in ligand stabilization for each case

(cc) BY

In contrast, compound **1c** presents a binding mode characterized by a balanced and cooperative network of interactions. The QTAIM analysis reveals significant contributions from E18 (0.0506 a.u.), L17 (0.0455 a.u.), and A12 (0.0439 a.u.), a multi-point anchoring that accounts for its exceptionally high ρ_{total} (0.2799 a.u.). This quantum-mechanical profile strongly correlates with the MM-PBSA data, where these residues also emerge as the primary energetic contributors. Such consistency between the two methods confirms that the stability of **1c** arises from an extensive electronic distribution across the binding pocket, although this high total density does not surpass the inhibitory potency of the reference compound.

Finally, the binding profile of compound **4c** (IC_{50} = 0.732 μM) reveals a highly localized and ultimately less efficient interaction pattern compared to the other derivatives. Both the MM-PBSA energetic decomposition and QTAIM topological analysis consistently identify residue E18 as the dominant anchoring site, exhibiting an exceptional energetic contribution of approximately -46.026 kJ mol^{-1} and an electron density of 0.0717 a.u., the highest recorded for any single residue in the series. However, despite the strength of this individual contact, **4c** displays the lowest total electron density ρ_{total} = 0.1736 a.u.), reflecting a marked deficiency in auxiliary stabilizing interactions within the active site. This lack of cooperativity is further evidenced in the per-residue decomposition plots, where, aside from the structural contact at the dimeric interface involving R472 (0.0078 a.u.), no significant contributions are observed from other key residues such as W21 or Y110. These findings suggest that for effective inhibition of *T. brucei* TR, a single "super-anchor" at E18 is insufficient to compensate for the absence of a distributed network of contacts, resulting in the weakest inhibitory potency observed among the studied compounds.

The integrated MM-PBSA and QTAIM analyses provide a comprehensive understanding of the molecular determinants required for effective inhibition of *Trypanosoma brucei* trypanothione reductase (TR). A fundamental conclusion is that inhibitory potency in this target is governed by the cooperativity and spatial distribution of the interaction network rather than the absolute strength of a single contact. While compound **4c** establishes the most robust individual interaction with residue E18 ($\Delta G \approx$ -46.02 kJ mol^{-1}; ρ = 0.0717 a.u.), its reliance on this singular "super-anchor" results in a lower total electron density and the weakest inhibitory activity (IC_{50}= 0.732 μM) among the series. In contrast, the superior potency of the reference compound M9J (IC_{50}= 0.120 μM) is driven by an optimized distribution of electronic density across key residues such as Y110 and W21, demonstrating that an energetically balanced "footprint" within Monomer 1 is critical for high-affinity binding. Furthermore, the consistent involvement of the dimeric interface (specifically through residues like R472) serves as a conserved structural anchor across all potent complexes, validating the requirement for inhibitors to bridge the two subunits of the enzyme. These findings suggest that future lead optimization should prioritize the recruitment of multiple medium-strength interactions distributed across the active site and the dimeric interface to achieve maximal inhibitory efficacy against *T. brucei* TR.

Importantly, the computational results consistently reflected the experimentally observed biological activities. The most active compounds generally exhibited the most favourable interaction patterns and binding free energies toward the proposed targets, whereas less active analogues formed weaker or less stable interactions. Collectively, these findings provide a molecular rationale for the observed structure-activity relationships and support the proposed target hypotheses.

Conclusions

In this study, we report novel hydroxynaphthalene and quinoline derivatives with potent activity against *Leishmania mexicana* and *Trypanosoma brucei*. Given the limited therapeutic options for these two parasitic infections, these findings are of significant interest from a medicinal chemistry perspective. Among the compounds reported the synthesized derivatives **1c**, **2c**, **2d**, and **4c** showed the most potent inhibitory

activities in the series; in fact, some of them showed inhibitory effects comparable to or even greater than the reference compounds. It is interesting to note that none of these compounds showed cytotoxic effects up to the highest concentration evaluated of 30 μM. Furthermore, these compounds fulfil Lipinski's Rule of Five and Veber's rules, with the exception of a slightly increased lipophilicity. In addition, the absence of detectable metabolism of compound **2c** in both rat and human liver microsomes indicates a high degree of microsomal stability and suggests a favourable metabolic profile that warrants further investigation in subsequent ADME studies. These physicochemical and metabolic characteristics make these compounds potential hit structures and interesting starting points for further development.

Regarding the possible molecular mechanism of action of these compounds as agents against *Leishmania mexicana*, although experimental corroboration is clearly necessary, our results obtained through molecular modelling studies allow us to propose two possible molecular targets. On the one hand, the possibility that these compounds act as inhibitors of the TR enzyme of *Leishmania mexicana* is very high in view of the similarity in the molecular behaviour obtained for the derivatives reported here and inhibitor H6H (the reference compound). On the other hand, our results also suggest that the active compounds in this series may inhibit Leishmania mexicana arginase, although through an alternative molecular mechanism.

In the search for a possible mechanism of action for our compounds as inhibitors of Trypanosoma brucei, our simulations suggest that these compounds act, at least in part, as inhibitors of its TR enzyme. In fact, our results clearly show that this is a very plausible mechanism of action for the hydroxynaphthalene and quinoline derivatives reported here.

Beyond identifying new active derivatives, the present study provides experimentally supported structure-activity relationships and possible molecular explanations for their biological activity, offering a rational basis for further optimization of this scaffold.

From a methodological standpoint, the combined use of docking, molecular dynamics simulations, and QTAIM calculations have proven to be a powerful approach for elucidating potential mechanisms of action of small ligands.

Supplementary material

Additional data are available at https://pub.iapchem.org/ojs/index.php/admet/article/view/3520, or from the corresponding author on request.

Author contributions: *Tomas Gonec: writing - review & editing, methodology, investigation, formal analysis, data curation; Tomas Strharsky: methodology, investigation; Marcela Vettorazzi: methodology, investigation; Lucas Gutierrez: methodology, investigation; Martina Cudova: methodology, investigation; Tereza Kauerova: methodology, investigation, formal analysis, data curation; Michaela Simurdova: methodology, investigation; Michal Oravec: methodology, investigation, formal analysis, data curation; Jiri Kos: writing - review & editing, writing - original draft, supervision, methodology; Peter Kollar: writing - review & editing, writing - original draft, validation, supervision, methodology, investigation, formal analysis, data curation; Bohuslav Drahos: writing - original draft, visualization, validation, methodology, investigation, formal analysis, data curation; Jan Jurica: methodology, investigation, formal analysis, data curation; Ondrej Zendulka: methodology, investigation, formal analysis, data curation; Jana Gregorova: investigation, data curation; Ondrej Pes: writing - review & editing, methodology, investigation, formal analysis, data curation; Joelle Quetin-Leclercq: writing - review & editing, methodology, investigation, formal analysis, data curation; Josef Jampilek: writing - review & editing, writing - original draft, visualization, validation, supervision, resources, project administration, methodology, formal analysis, data curation, conceptualization; Ricardo D. Enriz: writing - review & editing, writing - original draft, visualization, validation, supervision, resources, project administration, methodology, formal analysis, data curation, conceptualization.*

(cc) BY

Funding*: This work was supported by the Slovak Research and Development Agency [grants APVV-22-0133, APVV-24-0341, and APVV-24-0242]. M.O. acknowledges support from the Ministry of Education, Youth and Sports of the Czech Republic [project CzeCOS (LM2023048)]. B.D. acknowledges financial support from institutional sources of the Department of Inorganic Chemistry, Palacký University Olomouc, Czech Republic. This work was also partially funded by the Universidad Nacional de San Luis (UNSL, Argentina).*

Acknowledgements*: The authors are grateful to Maude Bourlet for her invaluable assistance with the antiparasitic assays. We also thank Alejandro Acuña for his technical support regarding cluster maintenance and computational assistance.*

Conflict of interest*: The authors declare no conflict of interest.*

Data availability*: The data supporting the findings of this study are available from the corresponding author upon reasonable request.*

References

[1] M.M. Meher, M. Afrin, A. Al Bayazid, M.S. Islam, M.Z. Ali. Deciphering the impact of heat wave in the global surge of infectious diseases. *Hygiene and Environmental Health Advances* **15** (2025) 100135. https://doi.org/10.1016/j.heha.2025.100135

[2] E. Zavaleta-Monestel, C. Rojas-Chinchilla, P. Molina-Sojo, M.F. Murillo-Castro, J.P. Rojas-Molina, E. Martínez-Vargas. Impact of climate change on the global dynamics of vector-borne infectious diseases: A narrative review. *Cureus* **17** (2025) e77972. https://doi.org/10.7759/cureus.77972

[3] A.J. Monaghan, K.M. Sampson, D.F. Steinhoff, K.C. Ernst, K.L. Ebi, B. Jones, M.H. Hayden. The potential impacts of 21st century climatic and population changes on human exposure to the virus vector mosquito Aedes aegypti. *Climatic Change* **146** (2018) 487-500. https://doi.org/10.1007/s10584-016-1679-0

[4] T. Iwamura, A. Guzman-Holst, K.A. Murray. Accelerating invasion potential of disease vector Aedes aegypti under climate change. *Nature Communications* **11** (2020) 2130. https://doi.org/10.1038/s41467-020-16010-4

[5] World Health Organization. Global Vector Control Response 2017-2030. World Health Organization, Geneva, Switzerland, 2017. Available at: https://www.who.int/publications/i/item/9789241512978 (accessed 25 June 2026).

[6] C. Tourapi, C. Tsioutis. Circular Policy: A New Approach to Vector and Vector-Borne Diseases' Management in Line with the Global Vector Control Response (2017-2030). *Tropical Medicine and Infectious Disease* **7**(7) (2022) 125. https://doi.org/10.3390/tropicalmed7070125

[7] F. Fouque, J.C. Reeder. Impact of past and on-going changes on climate and weather on vector-borne diseases transmission: A look at the evidence. *Infectious Diseases of Poverty* **8** (2019) 51. https://doi.org/10.1186/s40249-019-0565-1

[8] World Health Organization. Global Antimicrobial Resistance and Use Surveillance System (GLASS) Report: 2022. World Health Organization, Geneva, Switzerland, 2022. Available at: https://www.who.int/publications/i/item/9789240062702 (accessed 25 June 2026).

[9] World Health Organization. Neglected tropical diseases. Available at: https://www.who.int/health-topics/neglected-tropical-diseases#tab=tab_1 (accessed 25 June 2026).

[10] A. Ramsay, E.M. Kamau. Neglected Tropical Diseases Remain a Considerable Public Health Challenge in West Africa. *Tropical Medicine and Infectious Disease* **10**(3) (2025) 77. https://doi.org/10.3390/tropicalmed10030077

[11] A. Rodrigues, J.I. Weber, J. Durães-Oliveira, C. Moreno, M. Ferla, M. de Aires Pereira, A. Valério-Bolas, B.E. de Freitas, T. Nunes, W.T. Antunes, G. Alexandre-Pires, I. Pereira da Fonseca, G.M. Santos-Gomes. Extracellular vesicles derived from trypanosomatids: The key to decoding host-parasite communication. *International Journal of Molecular Sciences* **26**(9) (2025) 4302. https://doi.org/10.3390/ijms26094302

[12] C.M. Hollingshead, R. Bermudez. Human African Trypanosomiasis (Sleeping Sickness). In: *StatPearls*. StatPearls Publishing, Treasure Island, FL, USA, 2026. Available at: https://www.ncbi.nlm.nih.gov/books/NBK535413/ (accessed 25 June 2026).

[13] V. Lejon, A.K. Lindner, J.R. Franco. Human African trypanosomiasis. *The Lancet* **405** (2025) 937-950. https://doi.org/10.1016/S0140-6736(25)00107-2

[14] World Health Organization. Leishmaniasis fact sheet. Available at: https://www.who.int/news-room/fact-sheets/detail/leishmaniasis (accessed 25 June 2026).

[15] L. Maxfield, J.S. Crane. Leishmaniasis. In: *StatPearls*. StatPearls Publishing, Treasure Island, FL, USA, 2026. Available at: https://www.ncbi.nlm.nih.gov/books/NBK531456/ (accessed 25 June 2026).

[16] Editorial. Leishmania: an urgent need for new treatments. *eBioMedicine* **87** (2023) 104440. https://doi.org/10.1016/j.ebiom.2023.104440

[17] K.T. Angula, L.J. Legoabe, T. Swart, H.C. Hoppe, R.M. Beteck. Synthesis and in vitro antitrypanosomal evaluation of novel 6-heteroarylidene-substituted quinolone derivatives. *European Journal of Medicinal Chemistry* **227** (2022) 113913. https://doi.org/10.1016/j.ejmech.2021.113913

[18] K.M. de Santiago-Silva, B.T. da S. Bortoleti, L. do N. Oliveira, F.L. de A. Maia, J.C. Castro, I.C. Costa, D.B. Lazarin, J.L. Wardell, S.M.S.V. Wardell, M.G. Albuquerque, C.H. da S. Lima, W.R. Pavanelli, M. de L.F. Bispo, R.S.B. Gonçalves. Antileishmanial activity of 4,8-dimethoxynaphthalenyl chalcones on Leishmania amazonensis. *Antibiotics* **11**(10) (2022) 1402. https://doi.org/10.3390/antibiotics11101402

[19] C.B. Hartman, P.S. Dube, L.J. Legoabe, N. Van Pelt, A. Matheeussen, G. Caljon, R.M. Beteck. Novel quinoline derivatives with broad-spectrum antiprotozoal activities. *Archiv der Pharmazie* **357** (2024) e2300319. https://doi.org/10.1002/ardp.202300319

[20] Y. Pérez-Pertejo, J.M. Escudero-Martínez, R.M. Reguera, R. Balaña-Fouce, P.A. García, P.G. Jambrina, A. San Feliciano, M.-Á. Castro. Antileishmanial activity of terpenylquinones on Leishmania infantum and their effects on Leishmania topoisomerase IB. *International Journal for Parasitology: Drugs and Drug Resistance* **11** (2019) 70-79. https://doi.org/10.1016/j.ijpddr.2019.10.004

[21] M.V. de Araújo, P.S.O. de Souza, A.C. de Queiroz, C.B.B. da Matta, A.B. Leite, A.E. da Silva, J.A.A. de França, T.M.S. Silva, C.A. Camara, M.S. Alexandre-Moreira. Synthesis, leishmanicidal activity and theoretical evaluations of a series of substituted bis-2-hydroxy-1,4-naphthoquinones. *Molecules* **19**(9) (2014) 15180-15195. https://doi.org/10.3390/molecules190915180

[22] C. Galiana-Roselló, P. Bilbao-Ramos, M.A. Dea-Ayuela, M. Rolón, C. Vega, F. Bolás-Fernández, E. García-España, J. Alfonso, C. Coronel, M.E. González-Rosende. In vitro and in vivo antileishmanial and trypanocidal studies of new N-benzene- and N-naphthalenesulfonamide derivatives. *Journal of Medicinal Chemistry* **56** (2013) 8984-8998. https://doi.org/10.1021/jm4006127

[23] T. Gonec, J. Kos, I. Zadrazilova, M. Pesko, S. Keltosova, J. Tengler, P. Bobal, P. Kollar, A. Cizek, K. Kralova, J. Jampilek. Antimycobacterial and herbicidal activity of ring-substituted 1-hydroxynaphthalene-2-carboxanilides. *Bioorganic & Medicinal Chemistry* **21** (2013) 6531-6541. https://doi.org/10.1016/j.bmc.2013.08.030

[24] L. Vrablova, T. Gonec, P. Majerova, A. Kovac, D. Kos, P. Kollar, J. Kos, A. Cizek, T. Kauerova, J. Jampilek. Insight into antistaphylococcal effect of chlorinated 1-hydroxynaphthalene-2-carboxanilides. *ADMET and DMPK* **13** (2025) 2684. https://doi.org/10.5599/admet.2684

[25] L.E. Campos, F. Garibotto, E. Angelina, J. Kos, T. Gonec, P. Marvanova, M. Vettorazzi, M. Oravec, I. Jendrzejewska, J. Jampilek, S.E. Alvarez, R.D. Enriz. Hydroxynaphthalenecarboxamides and substituted piperazinylpropandiols, two new series of BRAF inhibitors: A theoretical and experimental study. *Bioorganic Chemistry* **103** (2020) 104145. https://doi.org/10.1016/j.bioorg.2020.104145

[26] R. Musiol, J. Jampilek, J.E. Nycz, M. Pesko, J. Carroll, K. Kralova, M. Vejsova, J. O'Mahony, A. Coffey, A. Mrozek, J. Polanski. Investigating the activity spectrum for ring-substituted 8-hydroxyquinolines. *Molecules* **15**(1) (2010) 288-304. https://doi.org/10.3390/molecules15010288

[27] J. Kos, I. Zadrazilova, E. Nevin, M. Soral, T. Gonec, P. Kollar, M. Oravec, A. Coffey, J. O'Mahony, T. Liptaj, K. Kralova, J. Jampilek. Ring-substituted 8-hydroxyquinoline-2-carboxanilides as potential

(cc) BY

antimycobacterial agents. *Bioorganic & Medicinal Chemistry* **23** (2015) 4188-4196. https://doi.org/10.1016/j.bmc.2015.06.047

[28] J. Kos, C.F. Ku, I. Kapustikova, M. Oravec, H.-J. Zhang, J. Jampilek. 8-Hydroxyquinoline-2-carboxanilides as antiviral agents against avian influenza virus. *ChemistrySelect* **4** (2019) 4582-4587. https://doi.org/10.1002/slct.201900873

[29] J. Kos, I. Kapustikova, C. Clements, A.I. Gray, J. Jampilek. 3-Hydroxynaphthalene-2-carboxanilides and their antitrypanosomal activity. *Monatshefte für Chemie - Chemical Monthly* **149** (2018) 887-892. https://doi.org/10.1007/s00706-017-2099-1

[30] T. Strharsky, D. Pindjakova, J. Kos, L. Vrablova, P. Smak, H. Michnova, T. Gonec, J. Hosek, M. Oravec, I. Jendrzejewska, A. Cizek, J. Jampilek. Trifluoromethylcinnamanilide Michael acceptors for treatment of resistant bacterial infections. *International Journal of Molecular Sciences* **23**(23) (2022) 15090. https://doi.org/10.3390/ijms232315090

[31] J. Kos, G. Degotte, D. Pindjakova, T. Strharsky, T. Jankech, T. Gonec, P. Francotte, M. Frederich, J. Jampilek. Insights into antimalarial activity of N-phenyl-substituted cinnamanilides. *Molecules* **27**(22) (2022) 7799. https://doi.org/10.3390/molecules27227799

[32] A. Bak, J. Kos, G. Degotte, A. Swietlicka, T. Strharsky, D. Pindjakova, T. Gonec, A. Smolinski, P. Francotte, M. Frederich, V. Kozik, J. Jampilek. Towards arginase inhibition: Hybrid SAR protocol for property mapping of chlorinated N-arylcinnamamides. *International Journal of Molecular Sciences* **24**(4) (2023) 3611. https://doi.org/10.3390/ijms24043611

[33] J. Kos, T. Strharsky, R. Tosso, L. Gutierrez, D. Kos, J. Jurica, O. Zendulka, O. Pes, J. Gregorova, G. Degotte, T. Gonec, M. Oravec, V. Vojackova, V. Krystof, A. Cizek, P. Francotte, M. Frederich, J. Jampilek, D. Enriz. Trifluoromethylcinnamanilides - Effective dual inhibitors of Mycobacterium smegmatis and Plasmodium falciparum. *Bioorganic Chemistry* **154** (2025) 107957. https://doi.org/10.1016/j.bioorg.2024.107957

[34] T. Gonec, J. Kos, I. Zadrazilova, M. Pesko, R. Govender, S. Keltosova, B. Chambel, D. Pereira, P. Kollar, A. Imramovsky, J. O'Mahony, A. Coffey, A. Cizek, K. Kralova, J. Jampilek. Antibacterial and herbicidal activity of ring-substituted 2-hydroxynaphthalene-1-carboxanilides. *Molecules* **18**(8) (2013) 9397-9419. https://doi.org/10.3390/molecules18089397

[35] T. Gonec, J. Kos, M. Pesko, J. Dohanosova, M. Oravec, T. Liptaj, K. Kralova, J. Jampilek. Halogenated 1-hydroxynaphthalene-2-carboxanilides affecting photosynthetic electron transport in Photosystem II. *Molecules* **22**(10) (2017) 1709. https://doi.org/10.3390/molecules22101709

[36] E. Spaczynska, A. Mrozek-Wilczkiewicz, K. Malarz, J. Kos, T. Gonec, M. Oravec, R. Gawecki, A. Bak, J. Dohanosova, I. Kapustikova, T. Liptaj, J. Jampilek, R. Musiol. Design and synthesis of anticancer 1-hydroxynaphthalene-2-carboxanilides with a p53 independent mechanism of action. *Scientific Reports* **9** (2019) 6387. https://doi.org/10.1038/s41598-019-42595-y

[37] G.M. Sheldrick. SHELXT - Integrated space-group and crystal-structure determination. *Acta Crystallographica Section A: Foundations and Advances* **71** (2015) 3-8. https://doi.org/10.1107/S2053273314026370

[38] O.V. Dolomanov, L.J. Bourhis, R.J. Gildea, J.A.K. Howard, H. Puschmann. OLEX2: A complete structure solution, refinement and analysis program. *Journal of Applied Crystallography* **42** (2009) 339-341. https://doi.org/10.1107/S0021889808042726

[39] C.F. Macrae, I.J. Bruno, J.A. Chisholm, P.R. Edgington, P. McCabe, E. Pidcock, L. Rodriguez-Monge, R. Taylor, J. van de Streek, P.A. Wood. Mercury CSD 2.0 - New features for the visualization and investigation of crystal structures. *Journal of Applied Crystallography* **41** (2008) 466-470. https://doi.org/10.1107/S0021889807067908

[40] J. Bero, V. Hannaert, G. Chataigné, M.-F. Hérent, J. Quetin-Leclercq. In vitro antitrypanosomal and antileishmanial activity of plants used in Benin in traditional medicine and bio-guided fractionation of the most active extract. *Journal of Ethnopharmacology* **137** (2011) 998-1002. https://doi.org/10.1016/j.jep.2011.07.022

[41] L. Molcanova, T. Kauerova, S. Dall'Acqua, P. Marsík, P. Kollar, K. Smejkal. Antiproliferative and cytotoxic activities of C-geranylated flavonoids from Paulownia tomentosa Steud. fruit. *Bioorganic Chemistry* **111** (2021) 104797. https://doi.org/10.1016/j.bioorg.2021.104797

[42] GraphPad Software. GraphPad Prism 5.00 software. Available at: http://www.graphpad.com (accessed 25 June 2026).

[43] R. De Gasparo, O. Halgas, D. Harangozo, M. Kaiser, E.F. Pai, R.L. Krauth-Siegel, F. Diederich. Targeting a large active site: Structure-based design of nanomolar inhibitors of Trypanosoma brucei trypanothione reductase. *Chemistry - A European Journal* **25** (2019) 11416-11421. https://doi.org/10.1002/chem.201901664

[44] A. Revuelto, M. Ruiz-Santaquiteria, H. de Lucio, A. Gamo, A.A. Carriles, K.J. Gutiérrez, P.A. Sánchez-Murcia, J.A. Hermoso, F. Gago, M.-J. Camarasa, A. Jiménez-Ruiz, S. Velázquez. Pyrrolopyrimidine vs imidazole-phenyl-thiazole scaffolds in nonpeptidic dimerization inhibitors of Leishmania infantum trypanothione reductase. *ACS Infectious Diseases* **5** (2019) 873-891. https://doi.org/10.1021/acsinfecdis.8b00355

[45] E.L. D'Antonio, B. Ullman, S.C. Roberts, U.G. Dixit, M.E. Wilson, Y. Hai, D.W. Christianson. Crystal structure of arginase from Leishmania mexicana and implications for the inhibition of polyamine biosynthesis in parasitic infections. *Archives of Biochemistry and Biophysics* **535** (2013) 163-176. https://doi.org/10.1016/j.abb.2013.03.015

[46] G.M. Morris, R. Huey, W. Lindstrom, M.F. Sanner, R.K. Belew, D.S. Goodsell, A.J. Olson. AutoDock4 and AutoDockTools4: Automated docking with selective receptor flexibility. *Journal of Computational Chemistry* **30** (2009) 2785-2791. https://doi.org/10.1002/jcc.21256

[47] C. Tian, K. Kasavajhala, K.A.A. Belfon, L. Raguette, H. Huang, A.N. Migues, J. Bickel, Y. Wang, J. Pincay, Q. Wu, C. Simmerling. ff19SB: Amino-acid-specific protein backbone parameters trained against quantum mechanics energy surfaces in solution. *Journal of Chemical Theory and Computation* **16** (2020) 528-552. https://doi.org/10.1021/acs.jctc.9b00591

[48] D.A. Case, H.M. Aktulga, K. Belfon, I.Y. Ben-Shalom, J.T. Berryman, S.R. Brozell, D.S. Cerutti, T.E. Cheatham III, G.A. Cisneros, V.W.D. Cruzeiro, T.A. Darden, N. Forouzesh, G. Giambaşu, T.J. Giese, M.K. Gilson, H. Gohlke, A.W. Götz, J.A. Harris, et al. AMBER 2024. University of California, San Francisco, CA, USA, 2024.

[49] D.A. Case, D.S. Cerutti, V.W.D. Cruzeiro, T.A. Darden, R.E. Duke, M. Ghazimirsaeed, G.M. Giambaşu, T.J. Giese, A.W. Götz, J.A. Harris, K. Kasavajhala, T.-S. Lee, Z. Li, C. Lin, J. Liu, Y. Miao, R. Salomon-Ferrer, J. Shen, R. Snyder, J. Swails, R.C. Walker, J. Wang, X. Wu, J. Zeng, T.E. Cheatham III, D.R. Roe, A. Roitberg, C. Simmerling, D.M. York, M.C. Nagan, K.M. Merz. Recent developments in Amber biomolecular simulations. *Journal of Chemical Information and Modeling* **65** (2025) 7835-7843. https://doi.org/10.1021/acs.jcim.5c01063

[50] Schrödinger LLC. The PyMOL Molecular Graphics System, Version 3.0. Schrödinger LLC, New York, NY, USA, 2015. Available at: https://www.pymol.org (accessed 25 June 2026).

[51] P. Li, K.M.J. Merz. MCPB.py: A Python Based Metal Center Parameter Builder. *Journal of Chemical Information and Modeling* **56** (2016) 599-604. https://doi.org/10.1021/acs.jcim.5b00674

[52] J. Wang, R.M. Wolf, J.W. Caldwell, P.A. Kollman, D.A. Case. Development and testing of a general AMBER force field. *Journal of Computational Chemistry* **25** (2004) 1157-1174. https://doi.org/10.1002/jcc.20035

[53] P. Mark, L. Nilsson. Structure and Dynamics of the TIP3P, SPC, and SPC/E Water Models at 298 K. *The Journal of Physical Chemistry A* **105** (2001) 9954-9960. https://doi.org/10.1021/jp003020w

[54] D.R. Roe, T.E. Cheatham III. PTRAJ and CPPTRAJ: Software for Processing and Analysis of Molecular Dynamics Trajectory Data. *Journal of Chemical Theory and Computation* **9** (2013) 3084-3095. https://doi.org/10.1021/ct400341p

[55] S. Genheden, U. Ryde. The MM/PBSA and MM/GBSA methods to estimate ligand-binding affinities. *Expert Opinion on Drug Discovery* **10** (2015) 449-461. https://doi.org/10.1517/17460441.2015.1032936

(cc) BY

[56] T. Lu, F. Chen. Multiwfn: A multifunctional wavefunction analyzer. *Journal of Computational Chemistry* **33** (2012) 580-592. https://doi.org/10.1002/jcc.22885

[57] L.J. Gutierrez, E. Angelina, A. Gyebrovszki, L. Fulop, N. Peruchena, H.A. Baldoni, B. Penke, R.D. Enriz. New small-size peptides modulators of the exosite of BACE1 obtained from a structure-based design. *Journal of Biomolecular Structure and Dynamics* **35** (2017) 413-426. https://doi.org/10.1080/07391102.2016.1145143

[58] L.J. Gutierrez, E.E. Barrera Guisasola, N. Peruchena, R.D. Enriz. A QM/MM study of the molecular recognition site of bapineuzumab toward the amyloid-β peptide isoforms. *Molecular Simulation* **42** (2016) 1-12. https://doi.org/10.1080/08927022.2015.1032276

[59] E. Vega-Hissi, R. Tosso, R.D. Enriz, L.J. Gutierrez. Molecular insight into the interaction mechanisms of amino-2H-imidazole derivatives with BACE1 protease: A QM/MM and QTAIM study. *International Journal of Quantum Chemistry* **115** (2015) e24854. https://doi.org/10.1002/qua.24854

[60] E.E. Barrera Guisasola, L.J. Gutiérrez, R.E. Salcedo, F.M. Garibotto, S.A. Andujar, R.D. Enriz, A.M. Rodríguez. Conformational transition of Aβ42 inhibited by a mimetic peptide: A molecular modeling study using QM/MM calculations and QTAIM analysis. *Computational and Theoretical Chemistry* **1080** (2016) 56-65. https://doi.org/10.1016/j.comptc.2016.02.002

[61] S. Rojas, O. Parravicini, M. Vettorazzi, R. Tosso, A. Garro, L. Gutiérrez, S. Andújar, R. Enriz. Combined MD/QTAIM techniques to evaluate ligand-receptor interactions. Scope and limitations. *European Journal of Medicinal Chemistry* **208** (2020) 112792. https://doi.org/10.1016/j.ejmech.2020.112792

[62] Advanced Chemistry Development, Inc. ACD/Percepta version 2025. Toronto, ON, Canada. https://www.acdlabs.com/products/percepta-platform/

[63] C.A. Lipinski, F. Lombardo, B.W. Dominy, P.J. Feeney. Experimental and computational approaches to estimate solubility and permeability in drug discovery and development settings. *Advanced Drug Delivery Reviews* **46** (2001) 3-26. https://doi.org/10.1016/S0169-409X(00)00129-0

[64] D.F. Veber, S.R. Johnson, H.-Y. Cheng, B.R. Smith, K.W. Ward, K.D. Kopple. Molecular properties that influence the oral bioavailability of drug candidates. *Journal of Medicinal Chemistry* **45** (2002) 2615-2623. https://doi.org/10.1021/jm020017n

[65] B.C. Doak, B. Over, F. Giordanetto, J. Kihlberg. Oral druggable space beyond the rule of 5: Insights from drugs and clinical candidates. *Chemistry & Biology* **21** (2014) 1115-1142. https://doi.org/10.1016/j.chembiol.2014.08.013

[66] M. Culen, A. Rezacova, J. Jampilek, J. Dohnal. Designing a dynamic dissolution method: A review of instrumental options and corresponding physiology of stomach and small intestine. *Journal of Pharmaceutical Sciences* **102** (2013) 2995-3017. https://doi.org/10.1002/jps.23494

[67] D.G. Jiménez, M. Vallaro, L. Vitagliano, L.L. López, G. Apprato, G. Ermondi, G. Caron. Molecular properties, including chameleonicity, as essential tools for designing the next generation of oral beyond rule of five drugs. *ADMET and DMPK* **12** (2024) 721-736. https://doi.org/10.5599/admet.2334

[68] Drug Hunter. Are Drugs Becoming More Lipophilic Over Time? Available at: https://drughunter.com/articles/are-drugs-becoming-more-lipophilic-over-time (accessed 25 June 2026).

[69] R.K. Sahu, J. Khan. Formulation strategies to improve the bioavailability of poorly absorbed drugs. In: *Advances and Challenges in Pharmaceutical Technology*, A.K. Nayak, K. Pal, I. Banerjee, S. Maji, U.B. Nanda, Eds., Academic Press, London, United Kingdom, 2021, pp. 229-242. https://doi.org/10.1016/B978-0-12-820043-8.00009-8

[70] D.S. Allgäuer, H. Jangra, H. Asahara, Z. Li, Q. Chen, H. Zipse, A.R. Ofial, H. Mayr. Quantification and theoretical analysis of the electrophilicities of Michael acceptors. *Journal of the American Chemical Society* **139** (2017) 13318-13329. https://doi.org/10.1021/jacs.7b05106

[71] S. Sundar, B. Singh. Emerging therapeutic targets for treatment of leishmaniasis. *Expert Opinion on Therapeutic Targets* **22** (2018) 467-486. https://doi.org/10.1080/14728222.2018.1472241

[72] K. Bora, M. Sarma, S.P. Kanaujia, V.K. Dubey. Dual-target drugs against Leishmania donovani for potential novel therapeutics. *Scientific Reports* **13** (2023) 18363. https://doi.org/10.1038/s41598-023-45448-x

[73] E. Persch, S. Bryson, N.K. Todoroff, C. Eberle, J. Thelemann, N. Dirdjaja, M. Kaiser, M. Weber, H. Derbani, R. Brun, G. Schneider, E.F. Pai, R.L. Krauth-Siegel, F. Diederich. Binding to large enzyme pockets: Small-molecule inhibitors of trypanothione reductase. *ChemMedChem* **9** (2014) 1880-1891. https://doi.org/10.1002/cmdc.201402032

[74] D.C. Jones, A. Ariza, W.-H.A. Chow, S.L. Oza, A.H. Fairlamb. Comparative structural, kinetic and inhibitor studies of Trypanosoma brucei trypanothione reductase with Trypanosoma cruzi. *Molecular and Biochemical Parasitology* **169** (2010) 12-19. https://doi.org/10.1016/j.molbiopara.2009.09.002

[75] H. de Lucio, A. Revuelto, A.A. Carriles, S. de Castro, S. García-González, J.C. García-Soriano, M. Alcón-Calderón, P.A. Sánchez-Murcia, J.A. Hermoso, F. Gago, M.-J. Camarasa, A. Jiménez-Ruiz, S. Velázquez. Identification of 1,2,3-triazolium salt-based inhibitors of Leishmania infantum trypanothione disulfide reductase with enhanced antileishmanial potency in cellulo and increased selectivity. *European Journal of Medicinal Chemistry* **244** (2022) 114878. https://doi.org/10.1016/j.ejmech.2022.114878

[76] V. Kourbeli, E. Chontzopoulou, K. Moschovou, D. Pavlos, T. Mavromoustakos, I.P. Papanastasiou. An overview on target-based drug design against kinetoplastid protozoan infections: Human African trypanosomiasis, Chagas disease and leishmaniases. *Molecules* **26**(15) (2021) 4629. https://doi.org/10.3390/molecules26154629

[77] P. Baiocco, G. Colotti, S. Franceschini, A. Ilari. Molecular basis of antimony treatment in leishmaniasis. *Journal of Medicinal Chemistry* **52** (2009) 2603-2612. https://doi.org/10.1021/jm900185q

[78] P. Baiocco, A. Ilari, P. Ceci, S. Orsini, M. Gramiccia, T. Di Muccio, G. Colotti. Inhibitory effect of silver nanoparticles on trypanothione reductase activity and Leishmania infantum proliferation. *ACS Medicinal Chemistry Letters* **2** (2011) 230-233. https://doi.org/10.1021/ml1002629

[79] F. Saccoliti, G. Angiulli, G. Pupo, L. Pescatori, V.N. Madia, A. Messore, G. Colotti, A. Fiorillo, L. Scipione, M. Gramiccia, T. Di Muccio, R. Di Santo, R. Costi, A. Ilari. Inhibition of Leishmania infantum trypanothione reductase by diaryl sulfide derivatives. *Journal of Enzyme Inhibition and Medicinal Chemistry* **32** (2017) 304-310. https://doi.org/10.1080/14756366.2016.1250755

[80] Neurosnap Inc. Powering Discovery Across Biology, Chemistry & Materials. Available at: https://neurosnap.ai/ (accessed 25 June 2026).

©2026 by the authors; licensee IAPC, Zagreb, Croatia. This article is an open-access article distributed under the terms and conditions of the Creative Commons Attribution license (http://creativecommons.org/licenses/by/4.0/)